Assembly of a beam target chamber for studying

screening potentials in condensed matter.

Joseph D. Hall

A senior thesis submitted to the faculty of
Brigham Young University
in partial fulfillment of the requirements for the degree of

Bachelor of Science

John E. Ellsworth, Advisor,

Department of Physics and Astronomy

Brigham Young University

August 2017

ABSTRACT

Assembly of a beam target chamber for studying
screening potentials in condensed matter.

Joseph D. Hall
Department of Physics and Astronomy, BYU
Bachelor of Science

The role of electron screening in condensed matter mediated nuclear fusion has been studied for decades. Nevertheless, the measured enhancements of the nuclear cross section are consistently greater than theoretical predictions, up to twice as large. We suspect that quantum fluctuations may cause this discrepancy. Described here is a vacuum system I have built to test this theory. This system enables target materials to be prepared and tested without exposing them to atmosphere. With the completion of this system, the future work will be to begin experimenting on materials to test our hypothesis.

ACKNOWLEDGMENTS

First and foremost, I'd like to thank my advisor and mentor John Ellsworth. Thank you for helping me figure out what needed to be done, and then helping me do it again after an unsuccessful attempt on my own. I'd also like to thank Alec Raymond for helping me whenever John wasn't around, and teaching me so much about detecting neutrons. I'd like to thank my wife Julie for her patience with me as I've worked on this project. Thank you for helping me with my presentations, showing an interest in my work, and just being a good support in general.

From the previous iteration of this thesis, I have mostly fixed inconsistencies in how I talked about the figures or deuterium (mainly syntax). There were a few places the text had been cut off, so I re-did those sentences. Perhaps most importantly, I tried to make my wording more descriptive and less ambiguous.

Contents

Chapter 1

Introduction

The goal of this work is to help discover the mysteries of electron screening in condensed matter mediated fusion. In essence, this is the process of embedding nuclear reactants in solid targets. In this chapter, a brief overview of fusion is given; including the roles of quantum tunneling and quantum electrodynamics. BYU's history with fusion is also explained.

1.1 The Unsolved Mystery of Electron Screening

Electron screening is a process in condensed matter that increases the probability of nuclear fusion; the increased probability depends on the target material. When the neighboring electrons in the target get close to the reactant, say hydrogen, the electron causes the hydrogen atom to appear less positive to a second hydrogen, reducing the repulsive force between them [1]. However, experiments have consistently yielded fusion rates larger than suggested by the theory of electron screening [1]. Therefore, while electron screening does aid in enhancing fusion, the experimental results suggest there may be another process involved. We still have no solid answer as to what this may be; this is the 30 year mystery of electron screening. In the Laboratory Nuclear Astrophysics Research (LNAR) group at Brigham Young University (BYU), we suspect the solution can be

found in the target's structure and the effects of quantum vacuum fluctuations. However, before explaining this process more in depth, background information regarding fusion is required.

1.2 Brief Introduction to Fusion

1.2.1 Fusion in the Sun

The energy radiated from stars comes from nuclear fusion. Within the core of stars, the strong gravitational force confines nuclei close together with enough energy to overcome the coulomb barrier, enabling fusion. The newly formed nuclei, however, are so energetic that they are unstable and promptly release their energy by blowing apart into smaller charged particles.

The determining factor of nuclear fusion is the separation distance between two nuclei. The nucleus is composed of neutrons and protons bound together. Individually, single protons and neutrons are referred to as nucleons. At first it may seem strange that nuclei can bind together, after all similarly charged particles repel each other. This repulsive force, F_c, is governed by Coulombs law

$$F_c = \frac{Z_1 \, Z_2 \, e^2}{r^2},$$
(1.1)

where Z_1 and Z_2 are the number of protons in each respective atom, e is the elementary charge, and r is simply the distance between them. However, there is a second attractive force called the strong force, which is responsible for the binding of nucleons. This force, which is more powerful than the Coulomb force, holds nucleons together and enables fusion. Yet the strong force decays much quicker than the Coulomb force with increasing separation. Thus fusion can only occur when two nuclei are brought close enough together that the strong force dominates. Figure 1.1 depicts the positive Coulomb barrier, which needs to be overcome to induce fusion, and the potential energy due to the strong force, represented by the blue vertical line. Note that the strong force is the determining force at close distances, on the order of fm (femtometers), but becomes insignificant
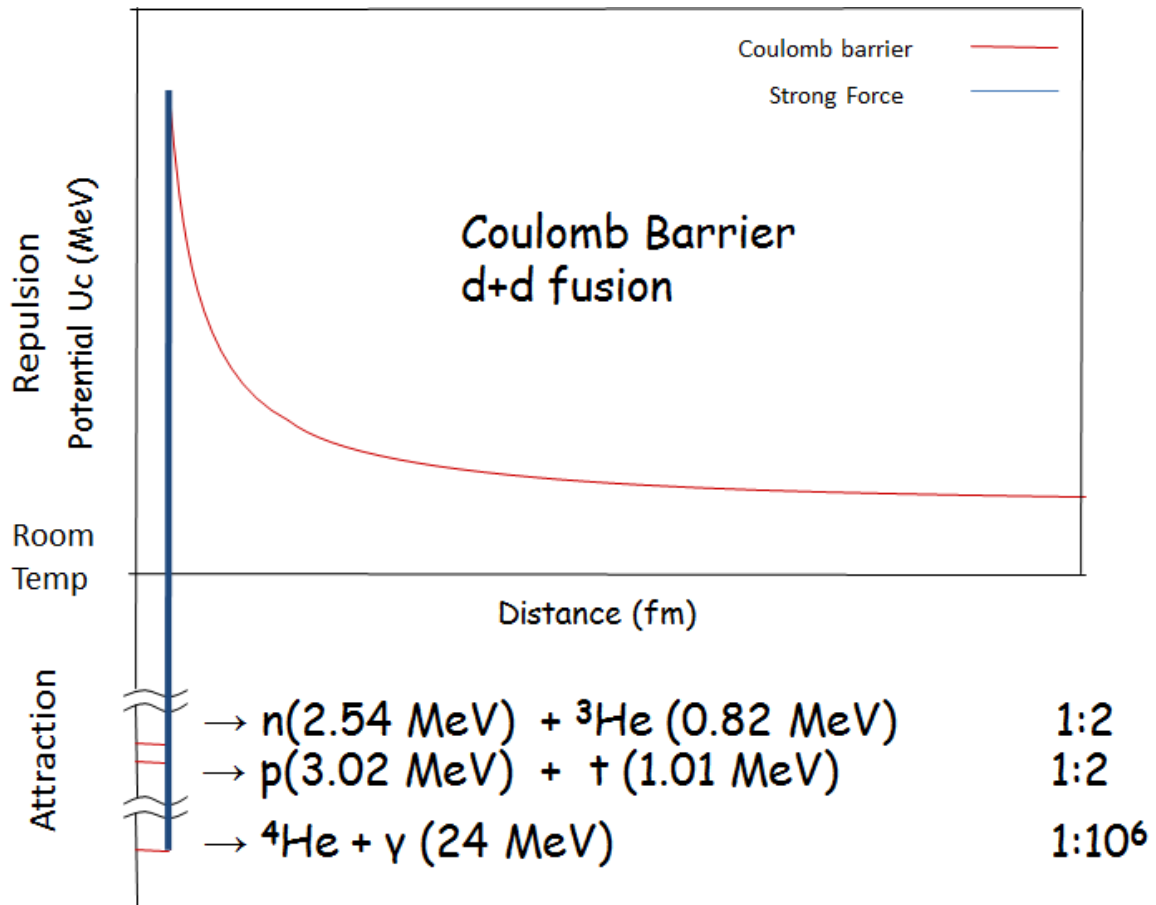
Figure 1.1 The Coulomb barrier has a much longer range than the strong force. Here, the strong force potential is represented by the vertical line that quickly becomes negative, representing a release of energy. Classically, a particle would need to follow the curve of the Coulomb barrier to its peak until the strong force takes over. Below the graph the possible products of d+d fusion are listed with their respective probabilities.

at large separations. Therefore, a classical particle needs a certain amount of energy to overcome the Coulomb barrier and fuse. In the case of two deuterium nuclei, $d + d$ fusion, the Coulomb barrier peak is around 440 keV in the center of mass (c.m.) frame.

It would appear, therefore, that fusion requires a significant amount of energy. Since fusion readily occurs within the sun, one might naively think that the sun's temperature can yield this amount of energy, but that is incorrect. At its peak, the temperature of the sun's core is around 1.5×10^7 Kelvin; relating that to energy via the Maxwell-Boltzmann distribution, and using the

mass of a deuteron, whose nuclei contains a proton and a neutron, the estimated energy is on the order of 1keV, significantly lower than the required 440 keV. To overcome the Coulomb barrier, deuterium would need temperatures on the order of a 5×10^9 Kelvin. The question then arises, how does fusion occur within the sun? The answer is found in quantum mechanics.

1.2.2 Quantum Tunneling

Quantum mechanics play a vital role in stellar fusion processes. From quantum mechanics, we know that every particle has an associated wave function, which corresponds to a probability density. What that means for these deuterons is that they don't have a specific location, rather they can be anywhere in a certain range. Specifically, there is a finite probability of finding them not only within the Coulomb potential, but also on the other side. This is called quantum tunneling, or barrier penetration.

Tunneling is certainly a quantum mechanical result; it is classically forbidden. Nevertheless, because of it, these deuterium particles can overcome the Coulomb barrier at relatively low energies and fuse, as shown in Figure 1.2. While not entirely true, one can think of tunneling as a low probability path that particles can take. In that context, rather than following the curve of the Coulomb barrier, a particle can instead go through the barrier, even at relatively low energies. Once at a close enough proximity, the strong force takes over and fusion occurs. At low energies, the probability, P, of penetrating the barrier can be approximated as

$$P = \exp(-2\pi\eta), \tag{1.2}$$

where η is the Sommerfield parameter given by

$$\eta = \frac{Z_1 Z_2 e^2}{\hbar v}. \tag{1.3}$$

Here, v is the magnitude of the relative incident velocity, and $\hbar$ is the reduced Planck constant. One should note that since $E \propto \sqrt{v}$ (where E is energy), the tunneling probability decays exponentially
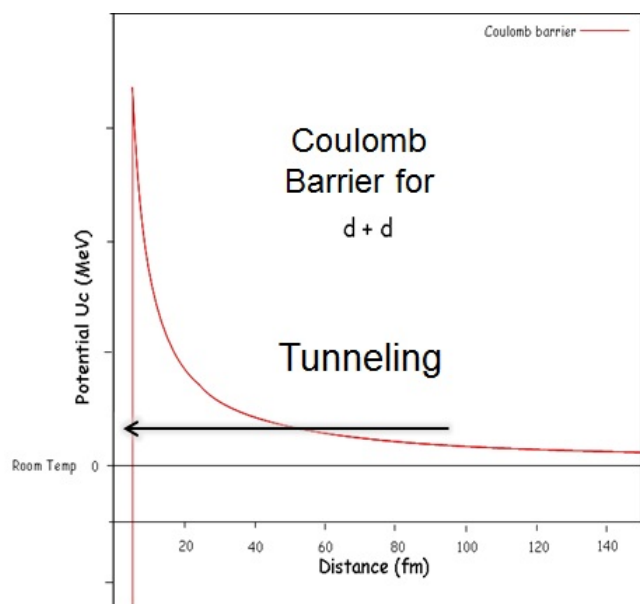
Figure 1.2 Quantum mechanical tunneling behavior. Classically a particle requires more energy than the barrier to overcome it. However, tunneling allows a particle with energy lower than the barrier to, in a sense, disregard the barrier. In doing so, nuclei can get much closer to each other, enabling fusion.

as energy decreases. If there is a high enough density of fusion reactants, tunneling becomes much more likely. It is through this quantum behavior that fusion occurs in stars.

1.2.3   Nuclear Cross Section and Astronomical S factor

As mentioned above, whether or not two particles interact is determined by probability. In nuclear reactions, one way to describe that probability is through the nuclear cross-sectional area. As a classical analog, one can relate it to a classical cross-sectional area. For example, when playing darts, it is much easier to hit a large target than a small one. Similarly, the nuclear cross-sectional area expresses the likelihood that two reactants "hit", or interact with each other. It is sufficient to know that the cross section is, in large part, determined by the c.m. energy of the reactants. As a result, at high energies the cross section is a very useful parameter in characterizing nuclear reactions. However, at stellar energies (1keV), the cross sections becomes increasingly asymptotic,
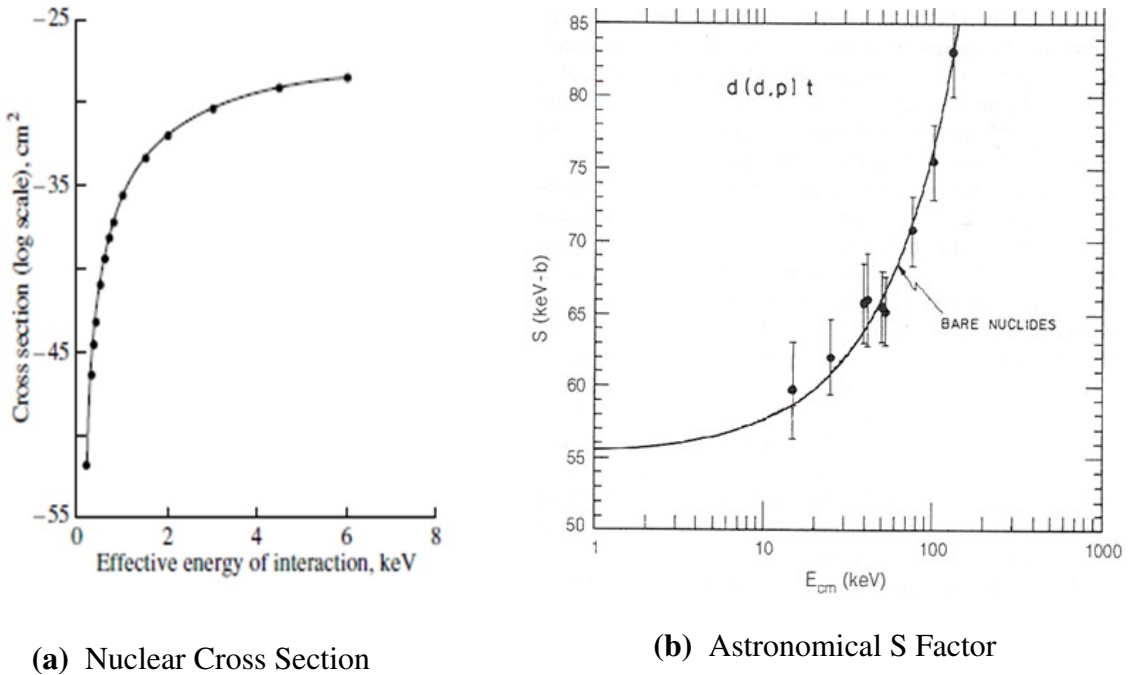
(a) Nuclear Cross Section **(b)** Astronomical S Factor

Figure 1.3 Cross-Section and S Factor vs Energy

The nuclear cross section (a) is asymptotic, and not useful at low energies, taken from [2]. The S factor (b) is a more insightful parameter than the cross section at low energies, as is explained more in depth later, taken from [3].

as shown in Figure 1.3a, making details indiscernible, so another description is needed.

At lower energies, it is more insightful to discuss the astronomical S factor. The S factor is found experimentally and contains all the uncertainties and unknowns in low energy reactions [4]. Essentially it is a re-scaling of the cross section, and as such, the S factor is similarly related to the interaction probability. In Figure 1.3b, one can see that the S factor is also asymptotic at low energies, nevertheless, it is a more informative parameter, as is shown later. While the S factor is of more importance to this work, understanding both the S factor as well as the nuclear cross section is useful in quantifying and describing fusion reactions in general.

1.3 BYU's Fusion History

Brigham Young University (BYU) has had a long history of nuclear fusion research. It began in the 1970s with Steven Jones and is led today by John E. Ellsworth. The Laboratory Nuclear Astrophysics Research (LNAR) group at BYU has been involved in many different fusion processes, such as muon catalzyed fusion, piezonuclear fusion, and metal catalyzed fusion. The following section describes these processes, and LNARs contributions, in more depth.

1.3.1 Muon Catalzyed Fusion

Muon Catalzyed Fusion (μCF) is a process that enables fusion to occur at low temperatures (room or cryogenic temperatures) as opposed to the 10^9 Kelvin needed to overcome the Coulomb barrier. A negative muon is similar to an electron in charge but is 206 times more massive [5], enabling it to act as a catalyst in inducing fusion. μCF was first observed in radiograph film in the 1940s but the observers could not classify the process [6]. At first, they could only conclude that some form of meson entered the film, induced a reaction, and was ejected again. In 1947, F.C Frank analyzed the particles momenta and energy and ruled out every possible reaction other than nuclear fusion induced by a muon [6]. In 1956, through the use of a hydrogen bubble chamber, Alvarez et al. proved Frank's conclusion [7]. They noticed that before decaying, several muons would come to rest, begin to move in a different direction, stop again, and so on. This odd path, highlighted in Figure 1.4, was evidence that fusion had occurred. In Figure 1.4 one sees a muon inducing fusion, then being ejected before it eventually decays. Alvares et.al. [7] hypothesized, and then observed, a single muon inducing multiple fusion events (releasing energy each time) before decaying.

So how does a muon induce fusion? In essence, the muon replaces an electron in a Hydrogen's molecular orbit. The mass of the muon causes a decrease in the average separation distance between the two nuclei by a factor of 200 [7]. This shrinks the Coulomb barrier and increases

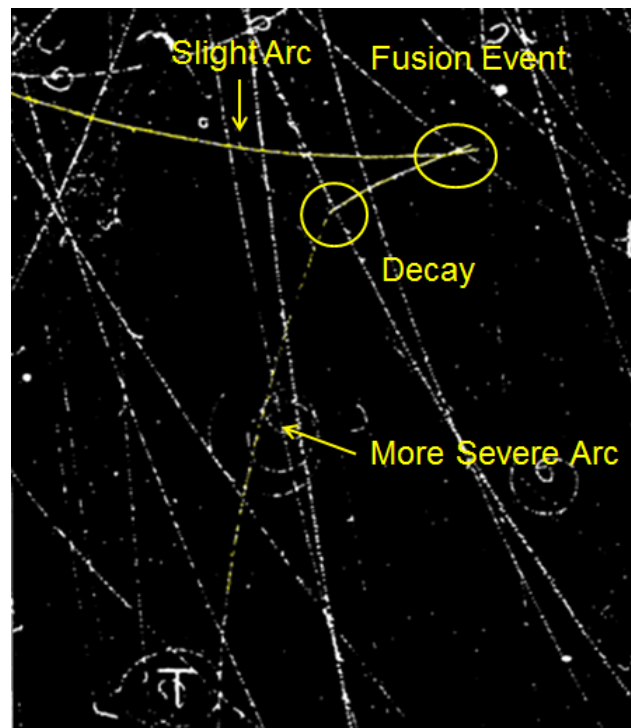**Figure 1.4** Traces from a hydrogen bubble chamber. The highlighted path is the muon, starting in the top left corner. In this picture, the muon induces a fusion event, and shortly thereafter decays. One can tell the muon has decayed into another particle because it abruptly changes direction and the arc of its trajectory becomes more severe indicating a less massive particle, borrowed from [7].
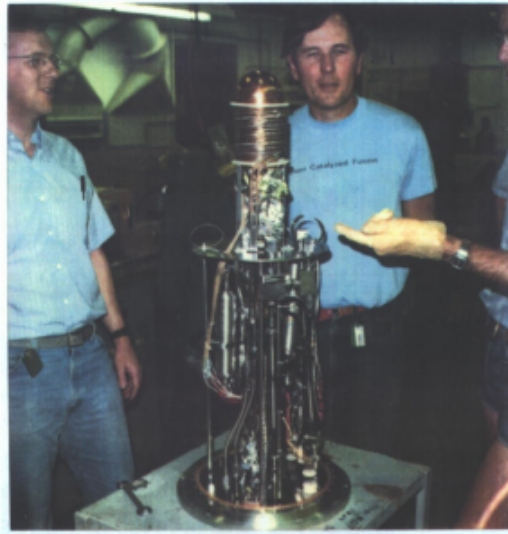
Figure 1.5 The system used by Steven Jones et. al. to achieve μCF. Shown here is here is Steven Jones (left), Guss Caffrey(center) and Mike Paciotti at the Los Alamos Meson Physics Facility. In this 1982 experiment, they got an average of 150 fusion reactions per muon, which is the highest to date.

the probability of tunneling. While this same process can occur in deuterium-deuterium reactions, deuterium-Tritium reactions are more frequent and release more energy so they showed the most potential.

At first μCF appeared to be the answer to the world's energy problems. The idea of a single muon being able to induce multiple fusion events is certainly appealing, but there are several problematic factors that, as of yet, (some 60 years later) have not been resolved. First, the lifetime of the muon in its own rest frame is only $2.2\mu s$ [5] and most of this time is spend wandering in between reactions; therefore, the muon is likely to decay before inducing too many events. Second, after each reaction, there is a 1% chance that the muon sticks on the resulting alpha particle, due to their opposite charges, removing it from possible future reactions [8]. Lastly, to reach industrial break-even (the output power is equal to the input power), each muon would need to induce, on average, 500 fusion events [8]. Even barring its short lifetime, it is currently impossible to mutually satisfy these two remaining problems. For example, Steven E. Jones, professor emeritus of BYU

and leading expert in μCF, was able to sustain 150 fusions per muon, the highest recorded rate to date but still well below the required 500 reactions per muon, see Figure 1.5. Therefore, even in the best of cases, the imperfections in energy and electrical transfer cause the output energy to fall far below "wall plug," or industrial, break-even levels (as explained above) [9]. So unless the energy required to produce muons is greatly reduced, μCF is not a viable energy resource.

1.3.2 Piezonuclear fusion

Piezonuclear fusion, coined by Steven Jones, is a method of inducing fusion through large pressures. The prefix "piezo" comes from a Greek word meaning to squeeze or compress [10]. In high pressure environments, such as the core of large planets, high pressures deform the Coulomb barrier, which in turn increases the probability of fusion. Jones et. al. [11] believe this process may, in part, account for the excess energy radiated by Jupiter. Jupiter emits 3/2 the amount of energy it absorbs from the sun, yet it is not massive enough to induce fusion as stars do [11]. Jones et al. speculated that within Jupiter's core, if the pressure is high enough, piezonuclear fusion may occur; resulting in a liquid-metal hydrogen core [11]. Nevertheless, due to the difficulty of achieving such high pressures experimentally, their results were inconclusive.

1.3.3 BYU Geo-Fusion Hypothesis and Vulcanology

Paul Palmer, another professor at BYU, suggested that a similar process of piezonuclear fusion may occur within earth's core as well. Jones, et. al. [12] conducted experiments in a laboratory by simulating conditions that may be found deep within the earth, and their results were promising. They were able to achieve d+d fusion in a way the earth may be able to induce naturally. To determine if fusion has occurred, one must detect certain charged particle products, in this case Tritium. Based on this idea, F. Goff and G.M. Murtry, a volcanologist and geophysicist respectively, took samples from ten different volcanic regions and tested their Tritium content [13]. Out
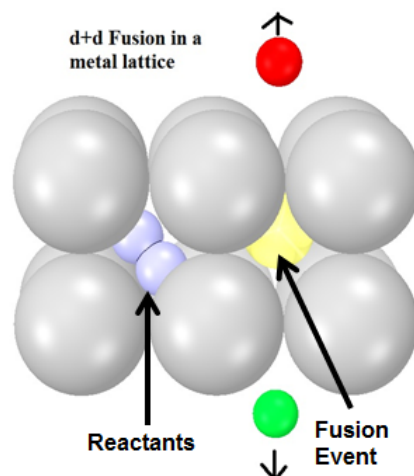
Figure 1.6 Illustration of how fusion in metals works. On the left side there are two fusion reactants (blue) in a metal lattice; the lattice decreases their separation distance and induces fusion. A reaction has occurred on the right, and products (red and green) are leaving the metal.

the ten samples tested, two had Tritium levels significantly above background. It is possible, as they state, that the excess Tritium levels may have come from nuclear testing in the surrounding areas [13]. However, tritium has a relatively low half-life, 12.4 years, so if the excess tritium is attributed to nuclear testing, after a half-life the levels should be significantly reduced. Since more than a half-life has passed since the study, we believe a revisit is necessary. If the Tritium levels have remained semi-constant over this time, it would indicate that "cold" fusion may in fact occur within the earth.

1.3.4   Metal Catalyzed Fusion

BYU was also a pioneer in experimenting with metals as catalysts to induce fusion. The main idea is to infuse metal with fusion reactants. Doing so forces the deuterons closer together, as illustrated in Figure 1.6; the free electrons in the metal make the deuterons appear less positively charged then they actually are. Thus the electrons act as a screen between the two deteurons,

Figure 1.7 The system in which Steve Jones induced metal catalyzed fusion.

increasing the probability of fusion. This is the process of electron screening in metals. To create a deuterated metal foil (a metal foil implanted with deuterium), the foil is placed in a vacuum, heated to enable out-gasing, then back-filled and pressurized with deuterium for a short period of time and then cooled; the flow of deuterium is controlled with the gas control system in Figure 1.8. Jones accomplished that process through the use the stainless steel tube furnace in Figure 1.7 [14]. By repeating the process at a higher temperature and pressure, the pressure within the chamber slowly decreases on its own [14]. This decrease in pressure indicates that deuterium was absorbed into the metal; it has now become deuterated, as evident by its increase in mass. When the system is perturbed through Joule heating (i.e. heating the metal by applying a current), charged particles and neutrons are detected, indicating fusion has occurred. This experiment, done by Steven Jones, yielded reaction rates of 6 fusions/mole of deuterium per second [14]. Metal catalyzed fusion is yet another fusion process that can occur at much lower temperatures than originally thought.
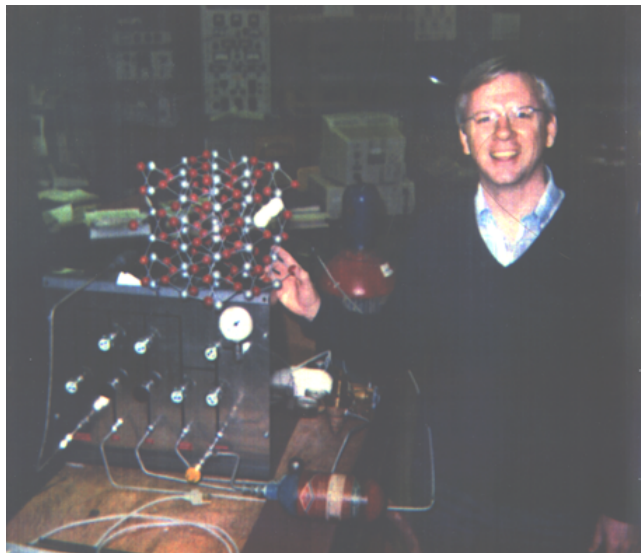
Figure 1.8 Steve Jones with the gas control system of the tube furnace and a model of the metal lattice.
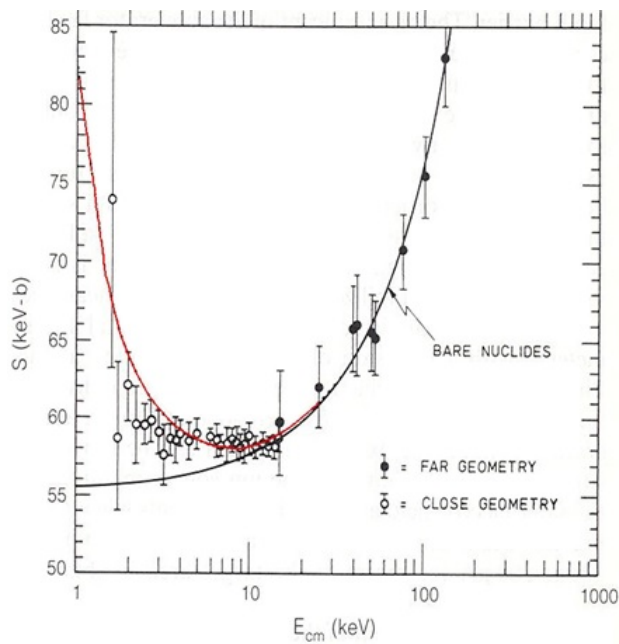

Figure 1.9 The S factor is greatly enhanced in electron screening. The black line is without screening, and the red line is with electron screening. Note that at energies above 20 keV, the enhancement factor is negligible [3].

1.3.5   LNAR Tested Materials and Potentials

While the basics of electron screening are understood, there is still a discrepancy between theorized fusion rates and experimentally found rates. The presence of electrons surrounding the nuclei increases the probability of tunneling, and enhances the cross section and S factor, as shown in Figure 1.9. Here the black line below 10keV is an extrapolation of the S factor without screening, and the red line with screening is significantly larger. The importance of the increased S factor is shown in Eq. 1.4. The enhanced factor, f, is defined as the ratio between cross sections (σ) for the screened and bare nuclei as follows (assuming a thin target) [15]:

$$f(E) = \frac{\sigma_{scr}}{\sigma_{bare}} = \frac{\frac{1}{E+U_e}S(E+U_e)\exp\left(-2\pi\eta\left(E+U_e\right)\right)}{\frac{1}{E}S(E)\exp\left(-2\pi\eta\left(E\right)\right)}. \tag{1.4}$$

Here, E represents the c.m. energy, η is the Sommerfield parameter (Eq. 1.3), S is the S factor, and U_e is the screening potential energy. It is important to note that f is related to the probability of fusion much like the cross section. Therefore, as the S factor increases, so does f, resulting in an increased probability of fusion. The U_e varies depending on the material (see Appendix A.1) and is responsible for the enhancement of the S factor as shown in Figure 1.9. To determine a material's screening potential, one measures the rates with and without electron screening, and then solves Eq. 1.4 for U_e. Refer to Appendix A.1 for a list of screening potentials.

1.4   Vacuum Quantum Electrodynamics

There is no such thing as a "true" vacuum; regardless of pressure attained there is a minimum energy and virtual particles. The purpose of this section is to show how those properties of a vacuum may affect condensed matter mediated fusion.

Virtual particles are similar to regular particles, but they exist for a very short time (having lifetimes on the order of femto seconds) due to the uncertainty principle [16]. The uncertainty principle relates uncertainties or ranges of energy and time by $\Delta E \Delta t \geq \hbar/2$. In a vacuum, therefore,

particle-antiparticle pairs can seemingly appear from nowhere, as long as they annihilate shortly thereafter [17]. Since their uncertainty in time is extremely small, they can take on almost any energy. One can think of the virtual particles as "borrowing" energy from the vacuum and then returning that same energy before any possible measurement can be made [17]. Therefore, not even a vacuum is an undisturbed state; the constant creation and destruction of virtual particles leads to quantum vacuum fluctuations.

These fluctuations lead to a minimum possible energy in a vacuum, the zero-point energy (ZPE). If it were possible to attain a "perfect" vacuum with no classical particles, the energy in that system would be zero. However, when we take into account the virtual particles of the vacuum, there arises energy unaccounted for classically; this is the ZPE. Max Planck was the first to suggest ZPE as a corrective term for the energy of photons with respect to the number of photons per electromagnetic (energy) mode, n. He originally derived that the energy E per mode of photon was given by

$$E = n\hbar\omega, \ \ with \ \ n = \frac{1}{\exp(\frac{\hbar\omega}{k_B T}) - 1} \tag{1.5}$$

where T is the temperature, and ω is the frequency [18]. However, several years later he resumed this work and came to a different result, namely that the energy is non-zero even as n goes to 0,

$$E = (\frac{1}{2} + n)\hbar\omega \tag{1.6}$$

[18]. While at first this derivation was met with skepticism, the study of ZPE and vacuum quantum electrodynamics (VQED) has increased dramatically. VQED has also led to many other theories and results including the Lamb shift, Casimir effect, spontaneous emission of light, and the Boyer theory of atomic stability. As Paul Davies, professor at Arizona State, has said, "empty space... holds the key to a full understanding of the forces of nature" [19].

A basic hydrogen atom consists of an electron orbiting around a proton, yet orbiting particles have acceleration and accelerating charged particles emit energy. This was one criticism with

Bohr's atomic model; eventually the electron should lose its energy and collapse into the proton. A quantum field theory explanation for why this doesn't happen is that the zero-point energy prevents this decay [20]. In 1987, Puthoff showed that the hydrogen ground state can be expressed as an equilibrium between the radiation emitted by the accelerating electron and the absorbed radiation from quantum vacuum fluctuations (QVF) [20]. The annihilation of virtual particles releases energy, which replenishes the electron enabling it to maintain an average equilibrium distance from the proton, this is called the Boyer theory [21]. However, it has been found that by imposing boundary conditions in the vacuum, the QVF are disrupted, altering the system.

By imposing boundary conditions in a vacuum, the energy density within the boundary becomes less than the energy density outside. Without the obstruction, all wavelengths of photons (generated by ZPE) are possible. Within the boundary however, the boundary conditions limit the possible wavelengths by requiring nodes at the boundary, similar to standing waves in a pipe. Perhaps the most common application of this is the Casimir Effect, in which two parallel plates in a vacuum experience and attractive force [22].

We now consider what happens to a hydrogen atom in such conditions. It has already been established that the Boyer theory of stability of the atom may arise from the ZPE through the absorption of photons in the vacuum. However, if a hydrogen atom were to be placed in boundary conditions, such as two parallel plates, the frequencies of these photons would be limited, so their energies would be as well. In such conditions, the electron may be unable to remain at its normal expectation value; its energy would not be fully replenished by the ZPE, but would find a new equilibrium much closer to the nucleus [23]. In this case, the electron would be more tightly bound to the atom, increasing its ionization energy, and causing a "modification of the ground-state energy" [24]. Similar to μCF, with an electron so close to the proton, the Coulomb barrier is lowered, increasing the probability of inducing fusion. Thus, it appears that VQED has applications in LNAR.

1.5 Electron Screening revisited

From this evidence it seems likely that the Boyer Theory can help explain the excess fusion rates obtained in electron screening experiments. In the process of thin film deposition, voids can often appear on the surface of the film. A void occurs when a section of the film does not grow like those around it, creating a sort of canyon in the deposited layer. It appears that these voids can act as parallel plates in modifying the deuterium particles in the same way they do for a ground state hydrogen [24]; we believe this is the answer to the 30 year mystery. To test this hypothesis, I have assembled a beam target chamber where thin films can be prepared and tested to find their screening potentials using Eq. 1.4. If this hypothesis is correct, we expect there to be a correlation between the shapes and number of voids in a material and its screening potential.

Chapter 2

Methods

In this section I describe the vacuum system used to find screening potentials. First the two chambers are described with their components. Then the charged particle and neutron detection methods are explained in addition to the velocity filter.

2.1   Accelerator Reaction Chamber

To study how voids on a target's surface affect screening potentials and fusion, I have assembled an accelerator reaction chamber. This chamber is suitable for this experiment because it allows us to prepare materials, through deposition or sputtering processes, and then test them without the films ever leaving vacuum. It consists of a deposition chamber coupled to a beam target chamber, as shown in Figure 2.1, each with its own turbo-pump.

As the name implies, the deposition chamber is where targets are prepared through deposition or sputtering (see Figure 2.2). Thermal deposition is a process used to coat a thin wafer, often times silicon, with another material, through the use of a thermal evaporation source. The desired material is placed in something akin to a tungsten bowl. By passing current through the tungsten and heating the source, the material begins to evaporate. While under vacuum, one places the target

18
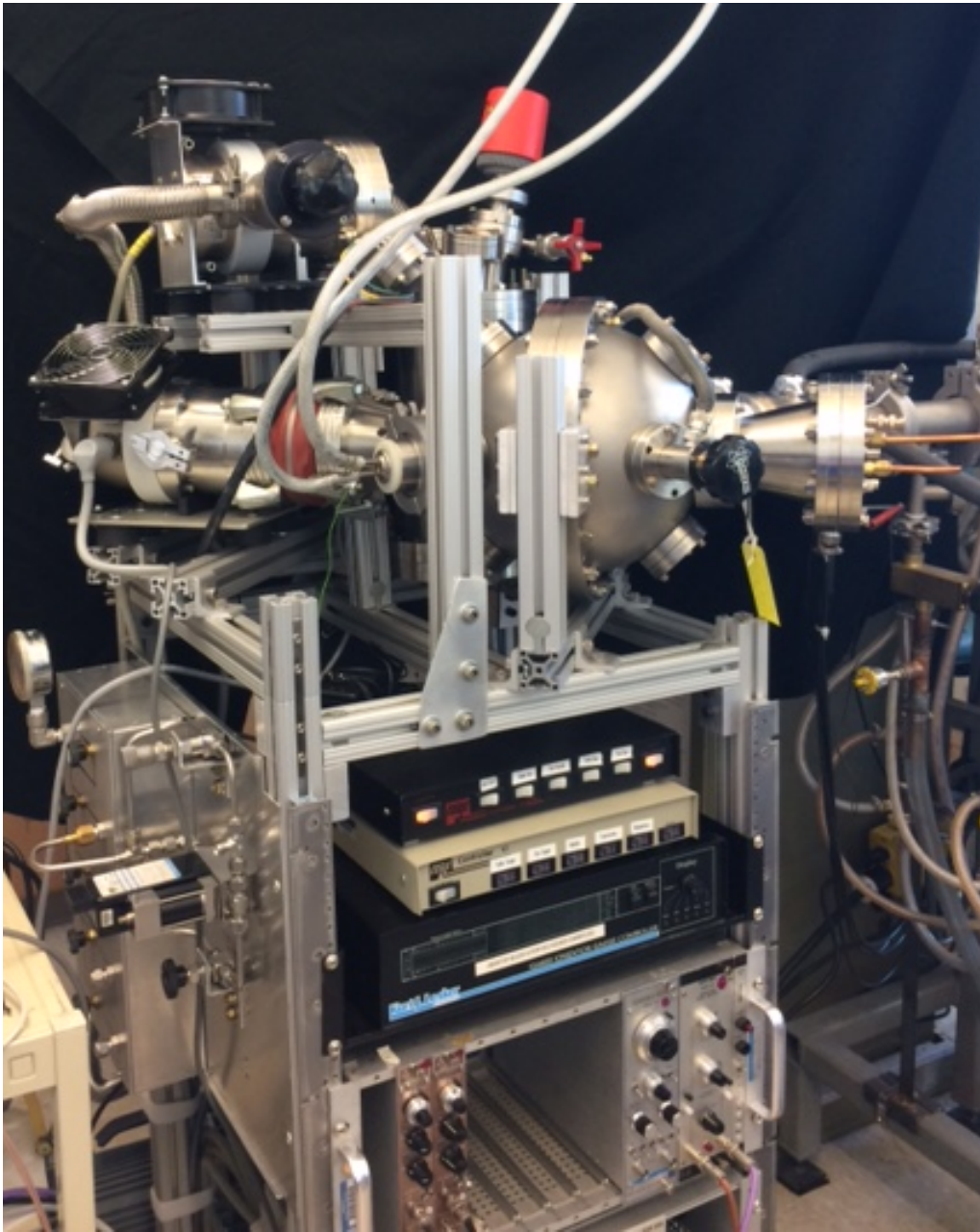
Figure 2.1 A current picture of the vacuum system. The front rack will be explained in depth in 2.11. The spherical chamber is the target chamber, shown again in Figure 2.4; the cylindrical deposition chamber (not visible) is directly behind it: see figure 2.2 for a better view. Refer to Appendix A.2 for a 3-D design of the chamber and A.3 for the method of assembly.

Figure 2.2 This cylindrical chamber is the deposition chamber, where materials are prepared. It consists of a turb-pump, a magentron, a Thermo-couple gauge (TC) and will connect to the gas flow system shown in Figure 2.3.

Figure 2.3 The gas flow system will allow us to control the introduction of reactive gases such as oxygen. In addition, it will enable us to back-fill the vacuum system with an inert gas, such as argon, rather than vent directly in air.

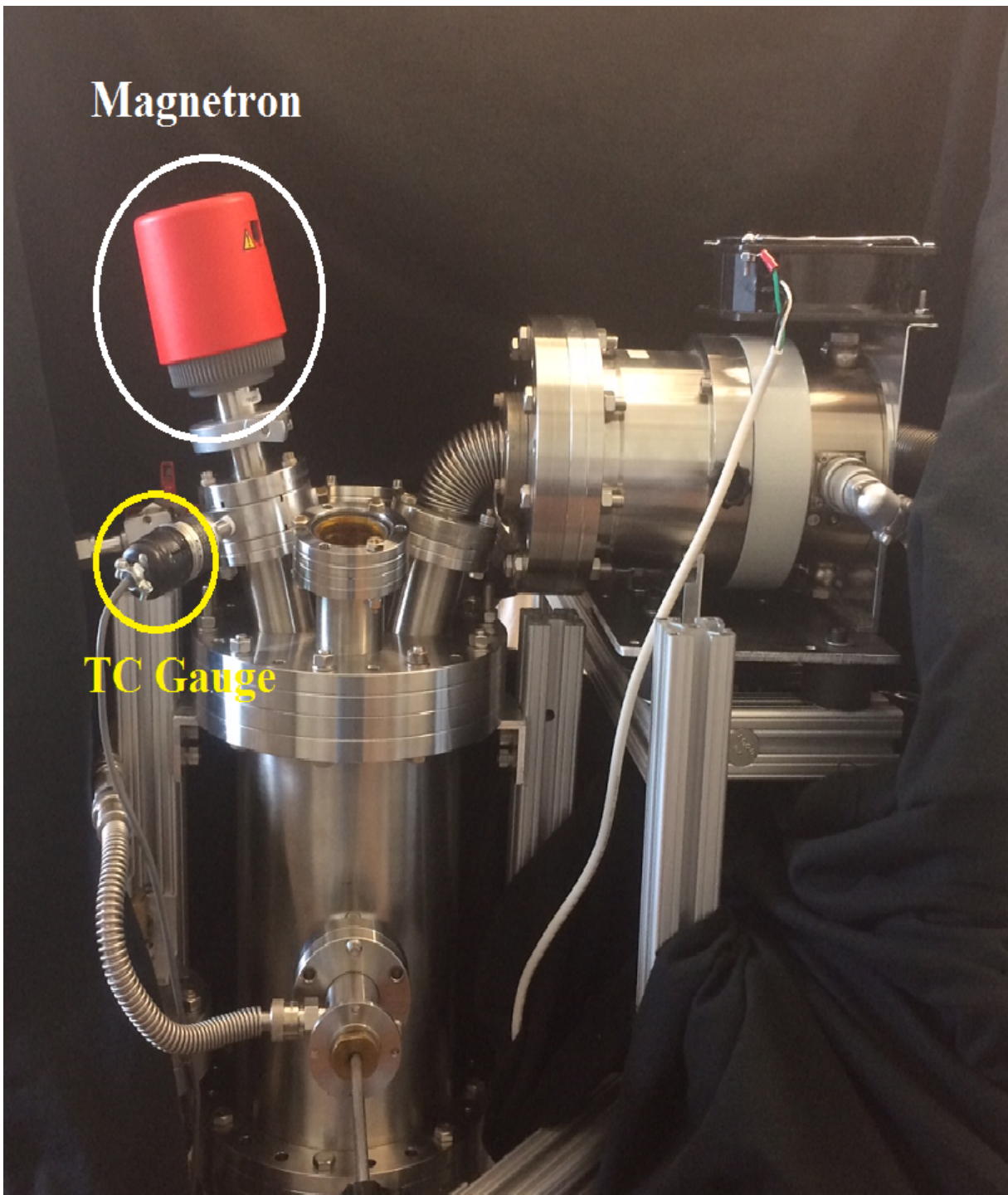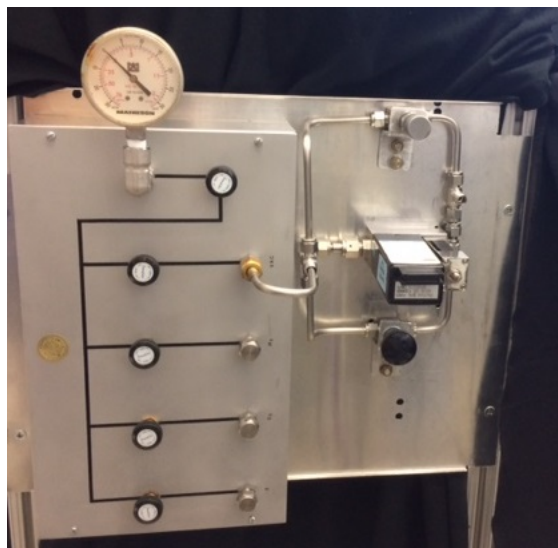substrate above a source then heats the source, coating the wafer in the evaporated material. Since the mean free path of particles is much longer in a vacuum, evacuating the deposition chamber ensures that the vapor actually reaches the wafer. The wafer is attached to the push rod shown in Figure 2.5, allowing it to move from the deposition to the target chamber once it has been prepared.

These films are then tested in the target chamber, Figure 2.4. In this chamber deuterium is accelerated towards the target (through the use of a particle accelerator shown in Figure 2.6), which causes them to become implanted into the target material. By connecting the deposition chamber to the target chamber, we have removed the need to expose the film to atmosphere in order to test it, thus eliminating the possibility of contaminating the film with oxygen, water, etc. However, connecting the chambers also runs the risk of contaminating the target chamber when preparing a target.

To avoid contaminating the target chamber, I have built a stopper shown in Figure 2.7 that is used to isolate the two chambers. The stopper consists of a sheet metal conical head connected
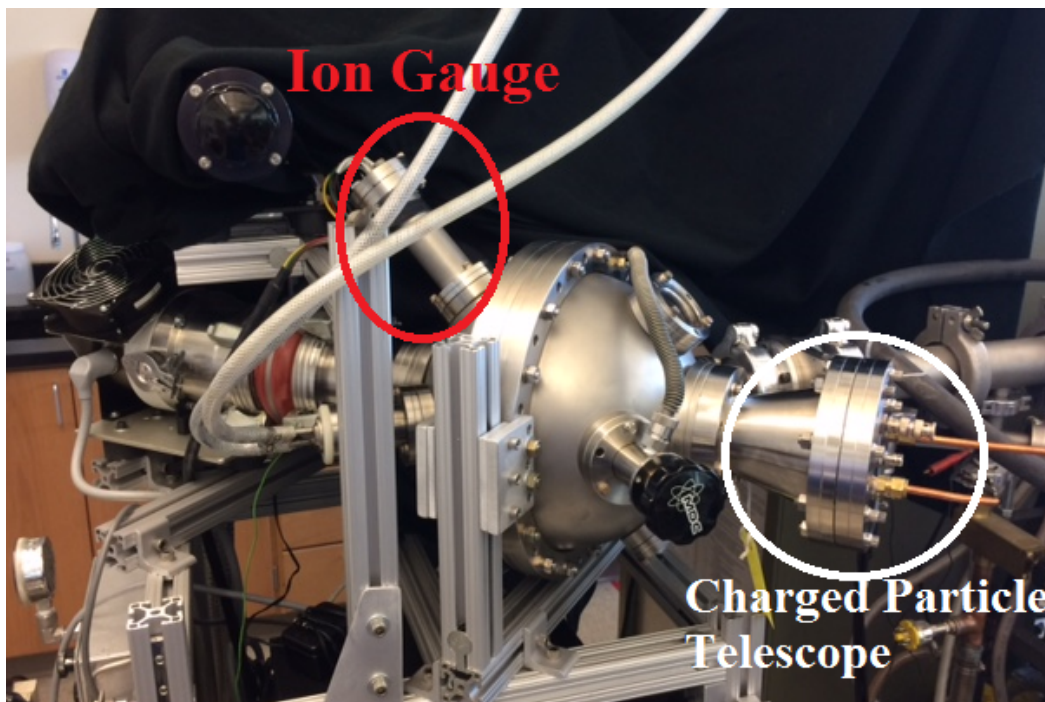
Figure 2.4 The beam target chamber connects to the accelerator shown in Figure 2.6 and is where materials are tested. It also connects to a turbo-pump, and houses the charged-particle telescope (Figure 2.13) and the stopper used to isolate the two chambers (Figure 2.7).
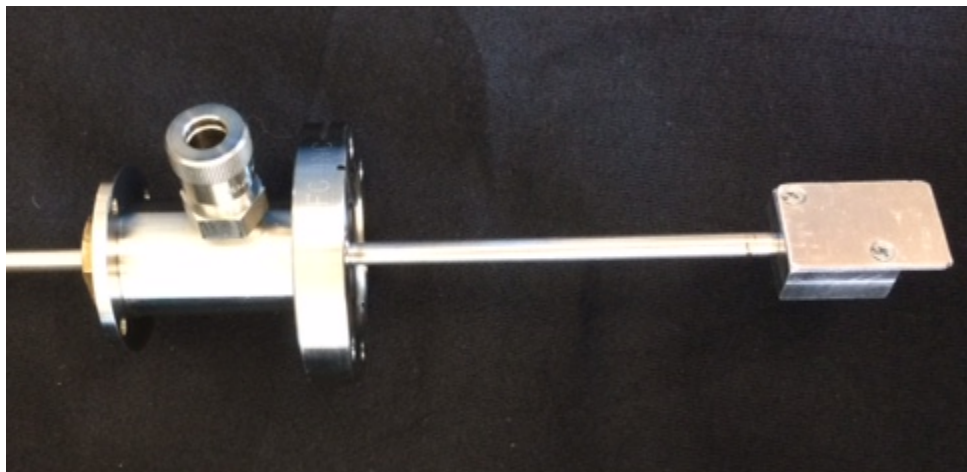
Figure 2.5 This rod can be retracted and extended in order to deposit and test respectively. In order to deposit a thin film, a silicon wafer is attached to the aluminum block shown in the picture. The rod is then inserted into the deposition chamber directly opposite the cone handle from Figure 2.7, and positioned above the carbon crucible which heats up and evaporates material onto the wafer. The rod can then be extended until it lays in the path of the accelerator beam.
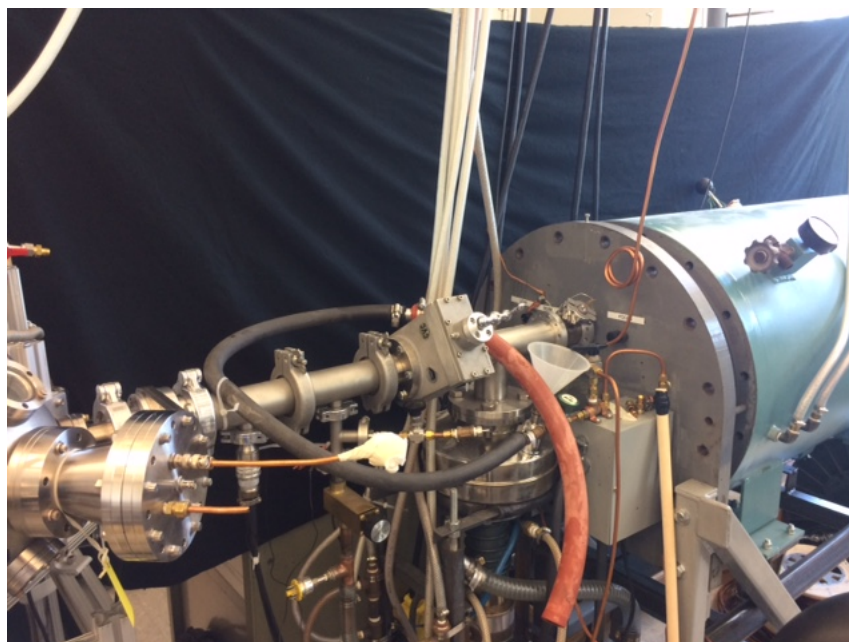
Figure 2.6 The vacuum system I constructed, on the left, connected to the particle accelerator with a separated by a gate valve, not visible. Using this accelerator, deuterium will be accelerated towards the target material at various energies, such as 10, 100, or 400keV.
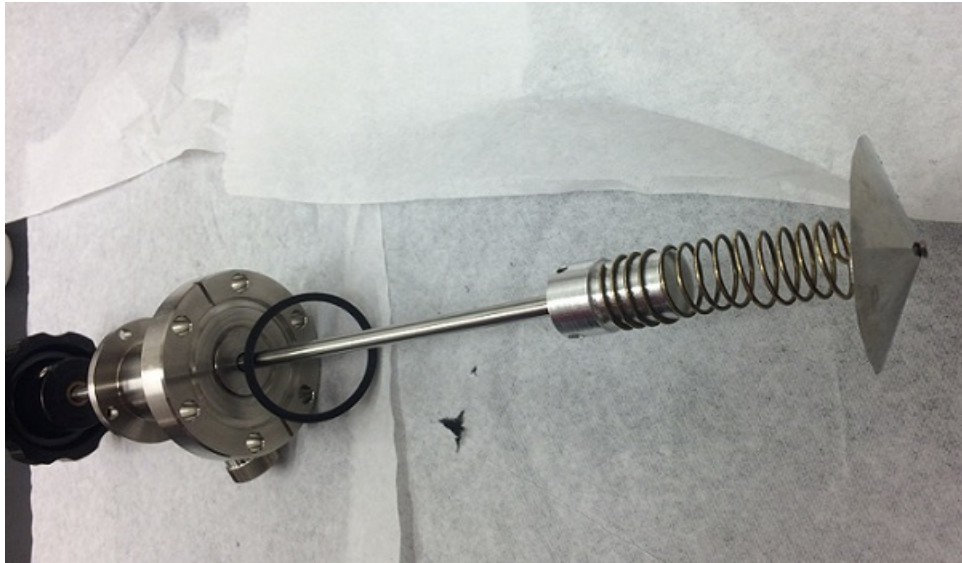
Figure 2.7 This device, similar to Figure 2.5, is used to separate the two chambers The spring on the end of the push rod enables the cone to slide into the correct position, blocking the connecting pathway between chambers.

to the push rod via a spring. Before depositing onto a wafer, the push rod is pushed fully into the target chamber. The spring allows the conical head to maneuver into the correct position; this blocks the path between the two chambers and prevents the coating material from contaminating the target chamber. When deposition is finished, it is simply extended outwards, and the film can be moved into the target chamber. While there are other ways to isolate the chambers, such as a gate valve, the push rod is ideal because it optimizes both price and weight.

2.2 Wien Filter

A Wien Filter, also known as a velocity selector, consists of perpendicular electric and magnetic fields of specific strengths to allow only particles of a certain velocity to pass through undeviated. To determine the strengths of the fields required, one simply sets the forces from both fields equal to each other, namely $qE = qv \times B$, where E and B are the electric and magnetic fields respectively,
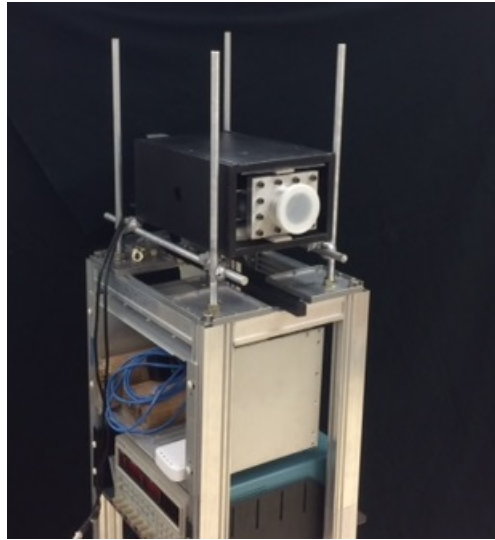
Figure 2.8 This Wien filter, or velocity selector, is totally contained in a thick, iron casing. The vacuum connection goes directly through the middle of the iron. Above and below the vacuum fitting are two permanent ceramic magnets. To the left and right of the fitting are two metallic plates with high voltage hook ups. I altered the filter slightly by inserting a steel plate in between either magnet and the vacuum fitting to decrease the magnetic field.

q is the charge of the moving particle and v is velocity. One can quickly see that the filtered velocity is then determined by the ratio v=$\frac{E}{B}$.

A few years ago, a student planned and built a Wien filter for a capstone project, Figure 2.8. The Wien filter consists of two permanent ceramic magnets and two plates to which a voltage can be applied, all encased in a solid iron container which helps to maintain a uniform magnetic field. This filter is an important addition to my vacuum system because it will help to filter out particles with unwanted energies coming from the particle accelerator. However, the magnetic field of the Wien filter, though uniform, was fairly strong, around .132 T as shown in figure 2.9. While this may not seem too strong at first, in order to filter out deuterium at 100 keV, we would need to apply a voltage of $\pm$5000 V to either end of the filter; Appendix A.7 shows the Mathematica code used for that calculation. Nevertheless, since the filtered velocity depends merely on their ration, any decrease in the B-field is matched by the E-field.
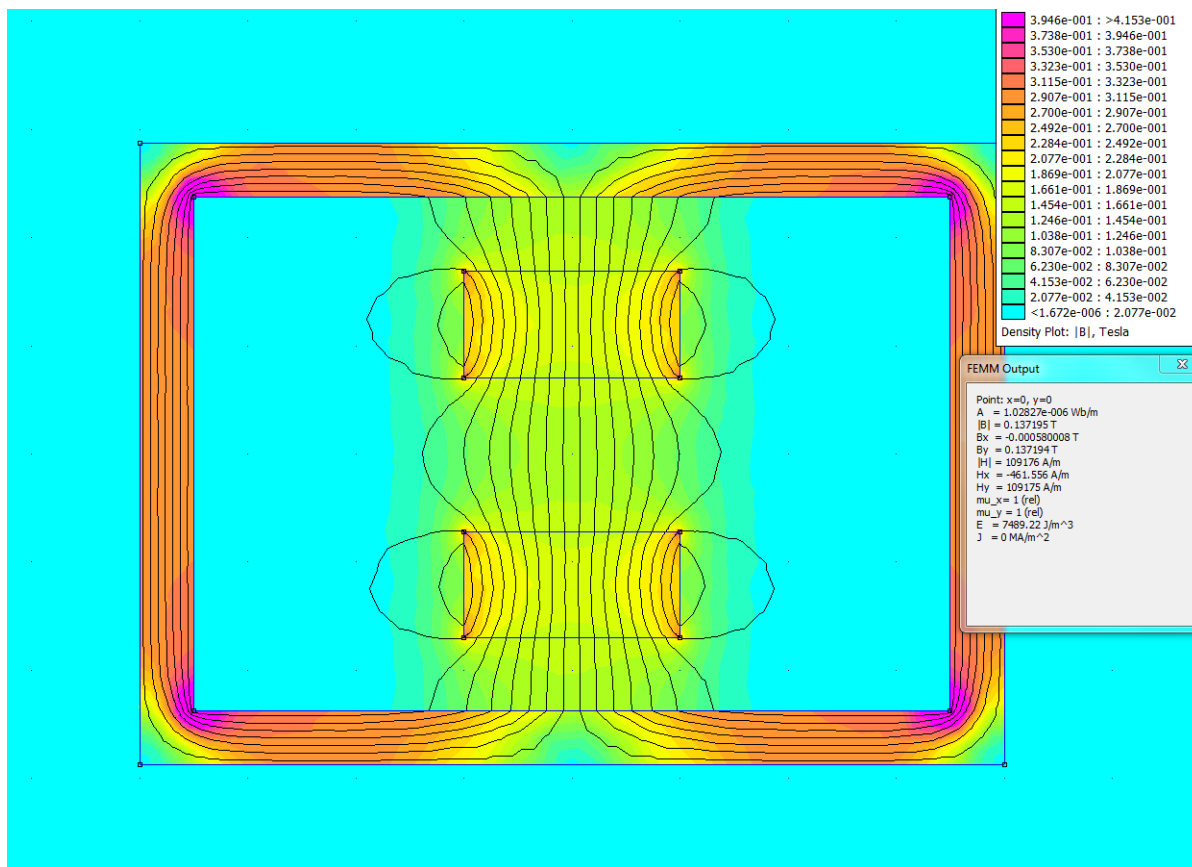
Figure 2.9 This image was rendered using Fem 4.2, a magnetic field simulation program using the original setup for the filter. It can easily be seen that the B-field is fairly uniform at the center between the two magnets. The smaller window on the right shows the details at the very center of the image, where the B-field is .137 T compared to the measured .132 T.

To that end, I inserted two $\frac{1}{8}$" steel plates inside the Wien filter that touch either end of the iron casing. Each plates is directly next to one of the two magnets. As a result, these plates decrease the B-field at the center of the filter by diverting more the of B-field lines directly to the iron casing. The resulting B-field is simulated in Figure 2.10, which shows a strength of .013 T. Even though the measured B-field didn't decrease as much as the simulation suggested, the measured value was .3 T after the changes, it was sufficient to lower the required voltage to ± 1200V from 5000V under the same conditions mentioned above.
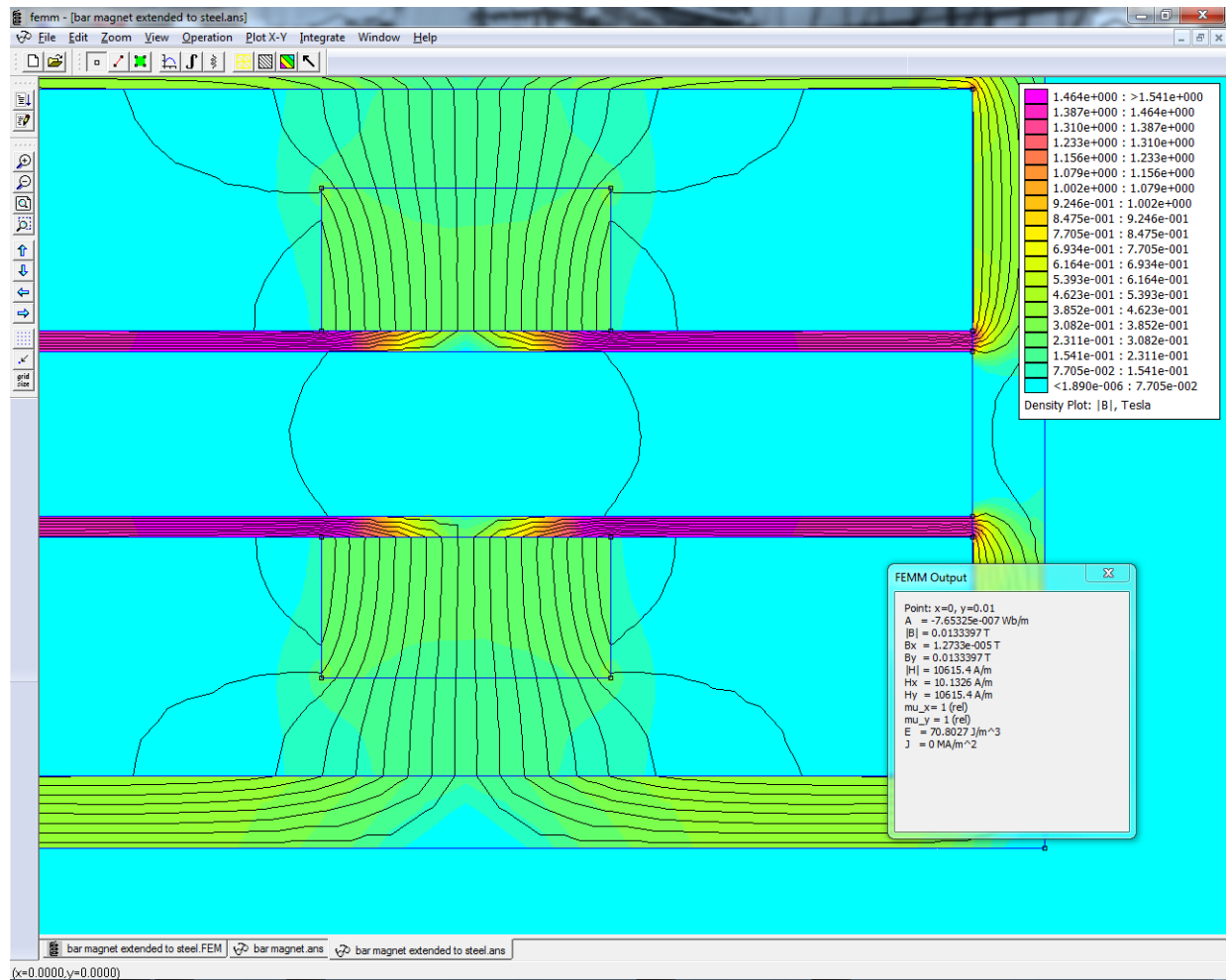
Figure 2.10 This image was rendered using Fem 4.2, a magnetic field simulation program after the steel plates were inserted. When compared to Figure 2.9, it would appear that the B-field is no longer uniform at the center, this is not accurate; the program simply omitted showing the B-field lines because they were much weaker than the surrounding areas. The smaller window on the right shows the details at the very center of image, where the B-field is .013 T compared to the measured .03 T.

2.3   Apparatus Used

Referring to Figures 2.2 and 2.4, there are three distinct pressure gauges connected to the deposition vacuum system: a thermocouple (TC) gauge, a magnetron, and an Ionization gauge. The TC gauge reads from atmosphere (around 760 Torr) to mTorr, while the magnetron and the Ion gauge read from mTorr to nTorr. The TC gauge and the Ion gauge connect to a Kurt J. Lesker Ionization gauge controller shown in Figure 2.11, which shows the pressure directly. I wired the magnetron to a power supply using the schematic in Appendix A.4, and connected it to a voltmeter. Rather than giving a direct pressure measurement, the magnetron outputs a voltage between 0-10V. The voltage output of the magnetron relates to pressure by the Pressure-Voltage table in Appendix A.5. All three gauges were tested on another vacuum system with calibrated gauges to ensure they read accurately. While the testing and deposition is done at high vacuum, around μTorr, the TC is needed to determine when the turbo-pumps can be turned on, since they should be off until about 50 mTorr. Through the use of turbo pumps, high vacuum is attainable; the resulting increase of the mean free path at high vacuum is necessary to detect fusion products and to produce reliable thin films.

Not visible in Figure 2.1 is the third, smaller turbo pump. This pump, shown in Figure 2.12, is used exclusively to constantly pump on the two push rods, from Figures 2.5 and 2.7. It connects directly to both of the push rod handles. When moving the push rods into or out of the chamber, there is a temporary breach of vacuum. This third pump is used to avoid that breach and ensure that the push rods don't introduce contaminants into the system.

2.3.1   Charged Particle Detection

To detect and analyze the charged particles from fusion reactions, we use a charged particle telescope. In Figure 2.1, the conflat cone with the copper pipes houses the charged particle telescope,

Figure 2.11 The top two bins are relays which power the everything on the system; it may be difficult to see but the switches are labeled according to what they power. Directly below them is the Ionization Gauge controller, which reads the pressure from the Ion gauge, as well as the thermocouples. The Nim Bim powers and amplifies the charged particle telescope described in 2.13. Lastly there are the three turbo pump controllers which power and monitor the speed of the turbo pumps.

Figure 2.12 The third turbo is used to evacuate and pump down the two push rod handles. When the push rods are moved, it causes a temporary breach of vacuum, introducing unwanted contaminants and causing a spike in pressure. However constant pumping on the handles avoids that.
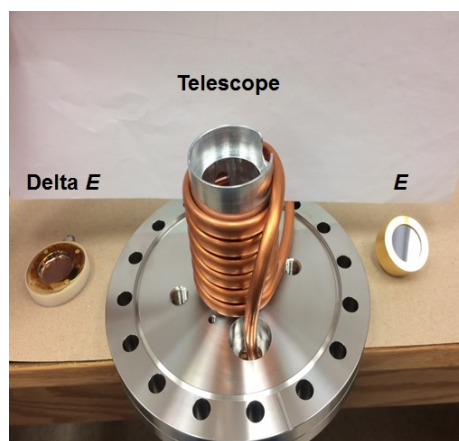
Figure 2.13 Charged particle telescope consisting of a ΔE on the left and a E detector on the right. The combination of these two detectors enables us to do basic spectroscopy. On top of the aluminum cylinder is an insulated copper mesh (not shown). A bias voltage applied to the mesh attracts charged particles to the telescope.
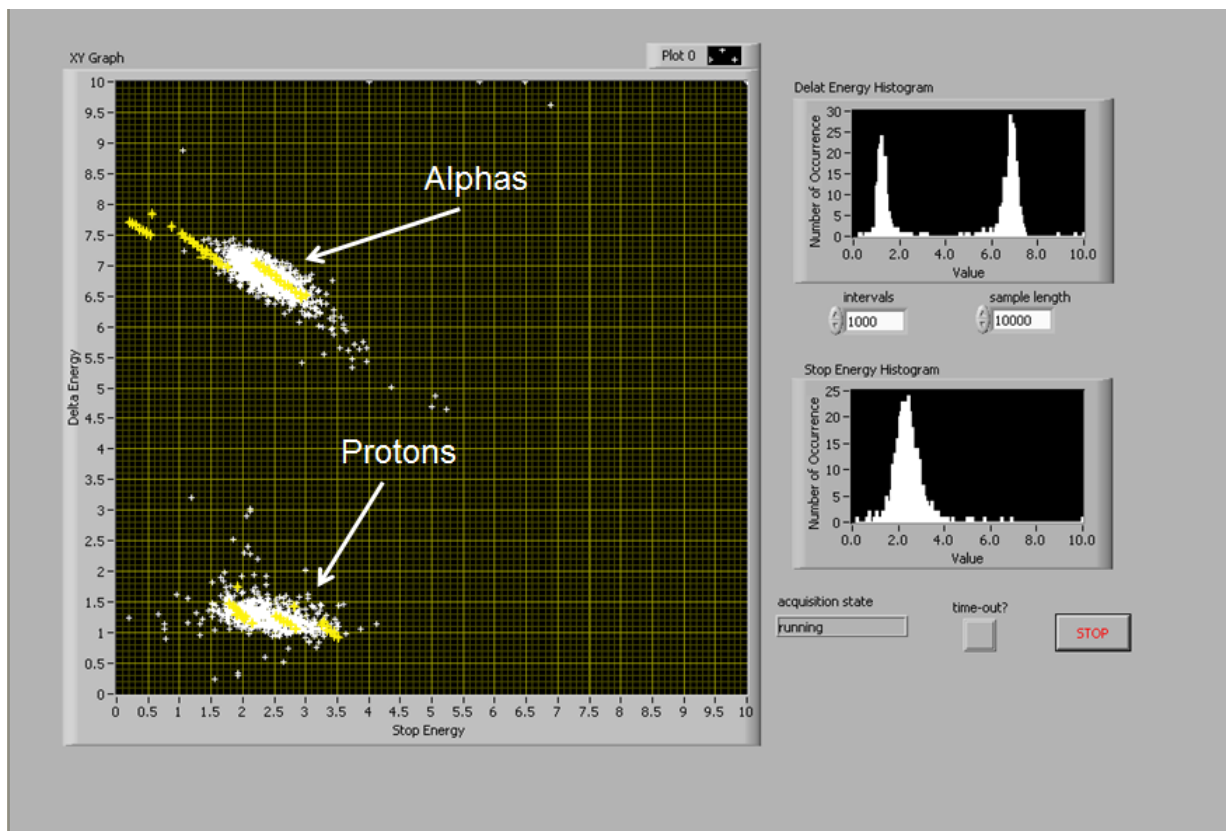
Figure 2.14 Data obtained from the telescope (the white dots) superimposed on a Monte Carlo simulation (the yellow dots). The y-axis is the energy deposited in the ΔE and the x-axis is the remaining E. Note that the alphas deposit significantly more energy in the first detector than the protons do.

which can be seen better in Figure 2.13. The telescope consists of two silicon surface barrier detectors placed in an aluminum cylinder coiled in a copper pipe. Liquid nitrogen flows through the pipe to cool the detectors and decrease noise. The thin detector on the left is the ΔE detector (with E referring to energy), meaning that when charged particles pass through it they deposit some of their energy into the detector. Particles then deposit the remainder of their energy and come to rest in the E detector: the thicker one on the right. By comparing the ΔE and E, we can determine what particle is detected and its approximate energy.

While the housing for the telescope is newly made, the detectors themselves have been used and
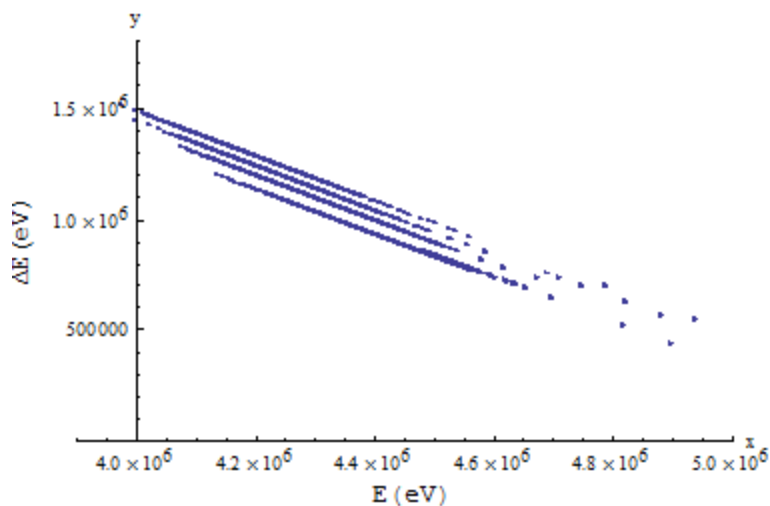
Figure 2.15 A SRIM output file analyzed on Mathematica. The y-axis represents the energy deposited in the ΔE detector and the x-axis represents the remaining energy detected in the E detector.

calibrated previously, mostly by John Ellsworth. To calibrate the detectors, they used a Stopping and Range of Ions and Matter (SRIM) program to simulate charged particles passing through the detectors. They then used alphas from an Am-241 source, and protons from a 2 MeV beam scattered by a thin tungsten wire to get a range of incident angles, as test particles to compare with the simulation. In Figure 2.14, data taken by the detectors is overlaid with the SRIM simulation; the ΔE and E are compared on a plot obtained using a LABVIEW interface. The alphas deposit significantly more energy in the first detector ΔE than protons do, enabling us to determine whether a fusion product was a proton or an alpha as a form of spectroscopy.

I used similar methods to what they did: namely, the use of a simulation and subsequent verification. The SRIM program simulates the penetrating depth of ions with given energies into a material. Here, the material is a 23.6 μm thick silicon surface barrier detector, the ΔE detector mentioned in the previous section. The energies of the alphas that come from the americium source were used for calibration. Americium 241 emits alphas with the energies shown in in Appendix A.6. Using those energies and our detector as the material, the SRIM program, analyzed by the

Mathematica code in Appendix A.8, yielded Figure 2.15.

Now that it has been several years, we needed to test the detectors again to ensure they work as desired. Thus, I removed the telescope from the chamber, attached the Am 241 source 1.5 inches from the front of the first detector, and attached the telescope directly to a roughing pump. By putting the source so close to the detector, we ensured a high number of counts on both detectors. The Detectors were powered by the Nim Bin, then the output signals were viewed on an oscilloscope and digitized through a Caen digitizer to be analyzed on a computer. Data was obtained both at room temperature and a while the detectors were chilled as liquid nitrogen flowed through the copper coil surrounding them shown in Figure 2.13. The set up is shown in Figure 2.16. The data is described further in Chapter 3.

2.3.2 Neutron Detection

To detect the emitted neutrons, we use two scintillators in conjunction with a Photo-Multiplier Tube (PMT), as shown in Figure 2.17. Scintillators are materials that emit light when charged particles move though them. As charged particles travel through a scintillator they radiate energy that is deposited into the molecules in the scintillator; this causes the molecules to become excited and consequently release their energy when they return to their initial state. The energy is released in the form of a light pulse which is detected by the PMT. Within the system shown in Figure 2.17, there are two scintillators; an organic hydrocarbon and a $Li_6Gd(B0_3)_3$:Ce or an LGB scintillator.

As emitted neutrons pass through the hydrocarbons in the organic scintillator, they recoil off the protons of similar mass. In doing so, they impart a significant amount of their energy to the proton; the proton then moves through the scintillator depositing energy and producing light pulses detectable by the PMT. Such pulses are referred to as proton recoils and they are narrow light pulses, as shown in Figure 2.18 .

After imparting much of its energy, the neutron is significantly slowed and "wanders" through
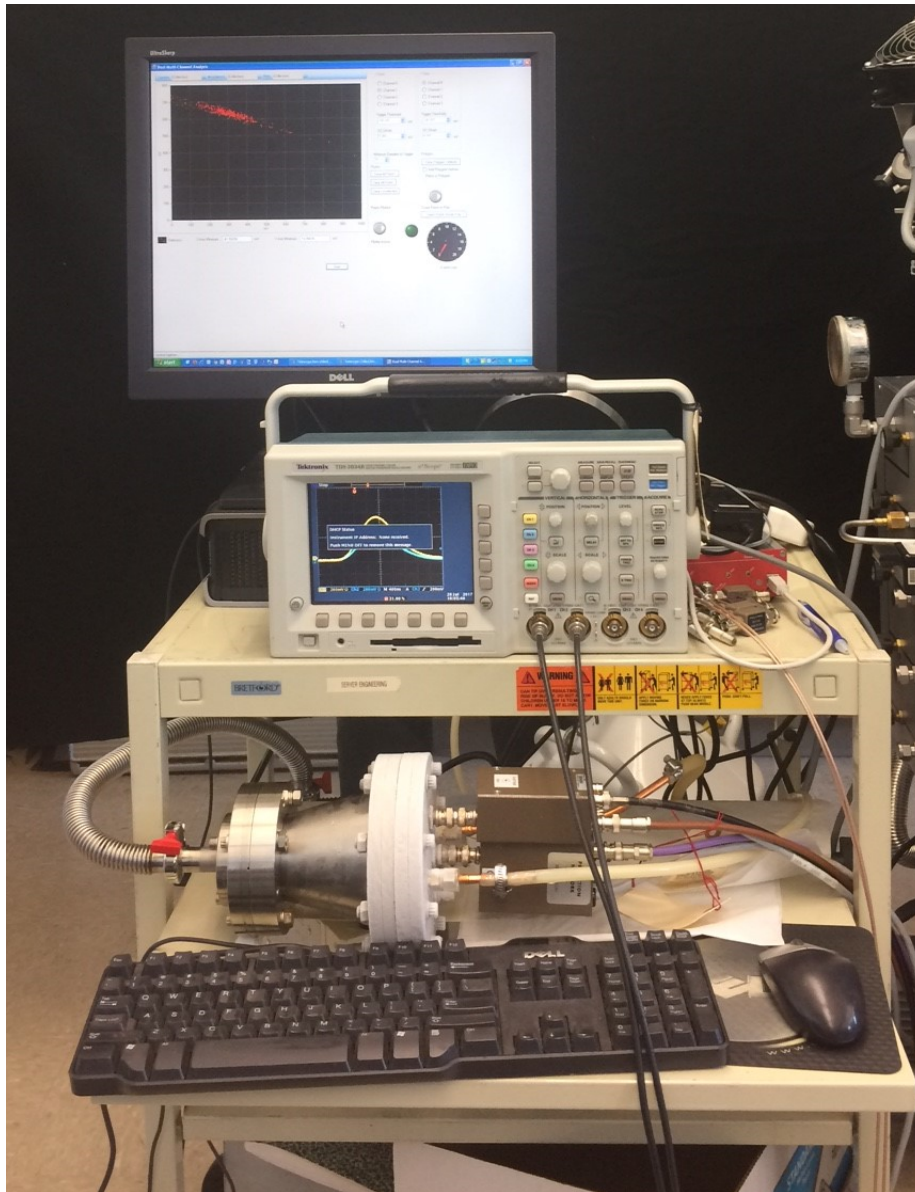
Figure 2.16 The configuration used to obtain data from the charged particle detectors. The oscilloscope is used to characterize the pulses and ensure they remain below 1V, the safety threshold of the digitizer. The analog output of the amplifier in Figure 2.11 is digitized on the digitizer and then analyzed on a program called Dual Mode Channel Analyzer, a program created by a previous student. Note that in this picture, the white covering on the base of the conflat cone is frozen, condensed water: indicating the detectors are being chilled.
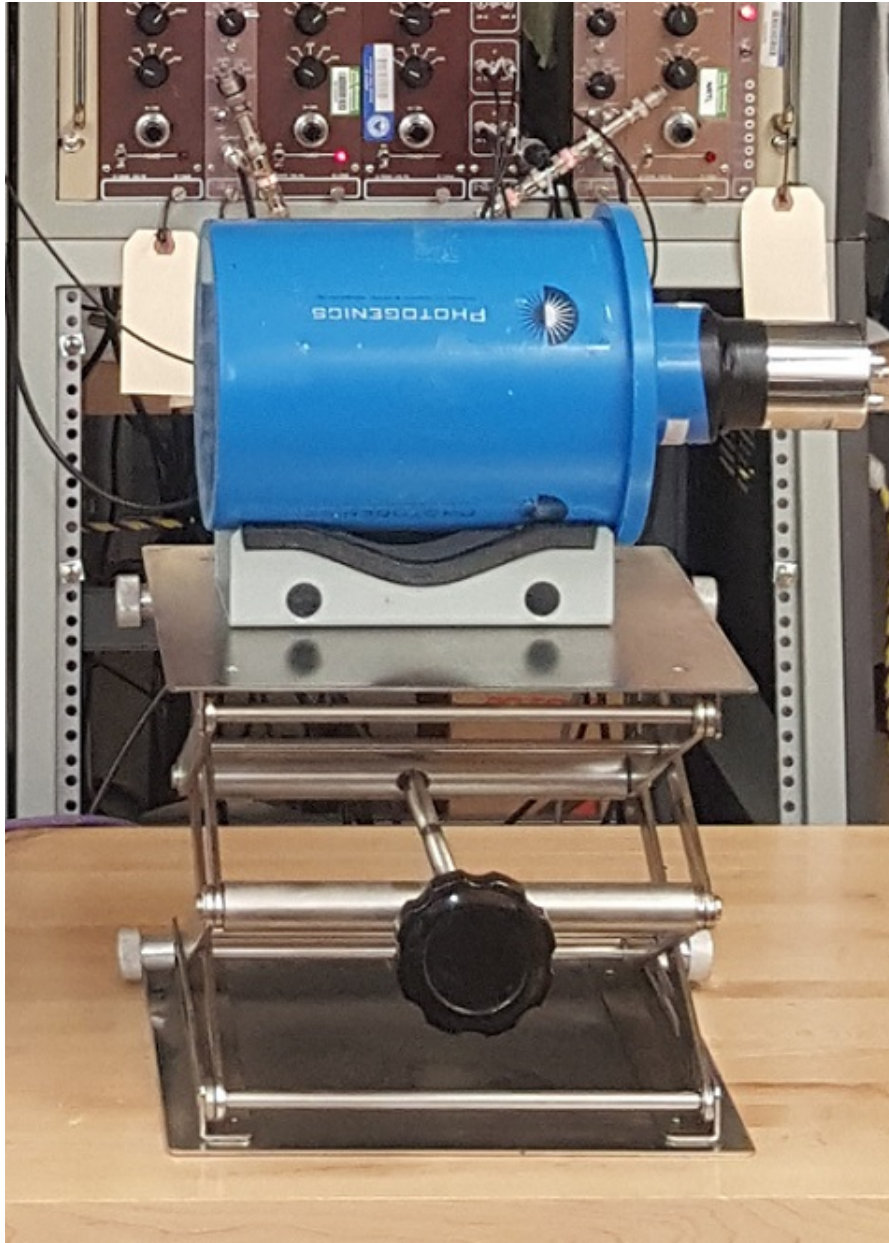
Figure 2.17 This detector houses two different scintillators connected to a PMT. The combination of the two scintillators enables neutrons to be detected, see Figure 2.18 for an example of the PMT output.
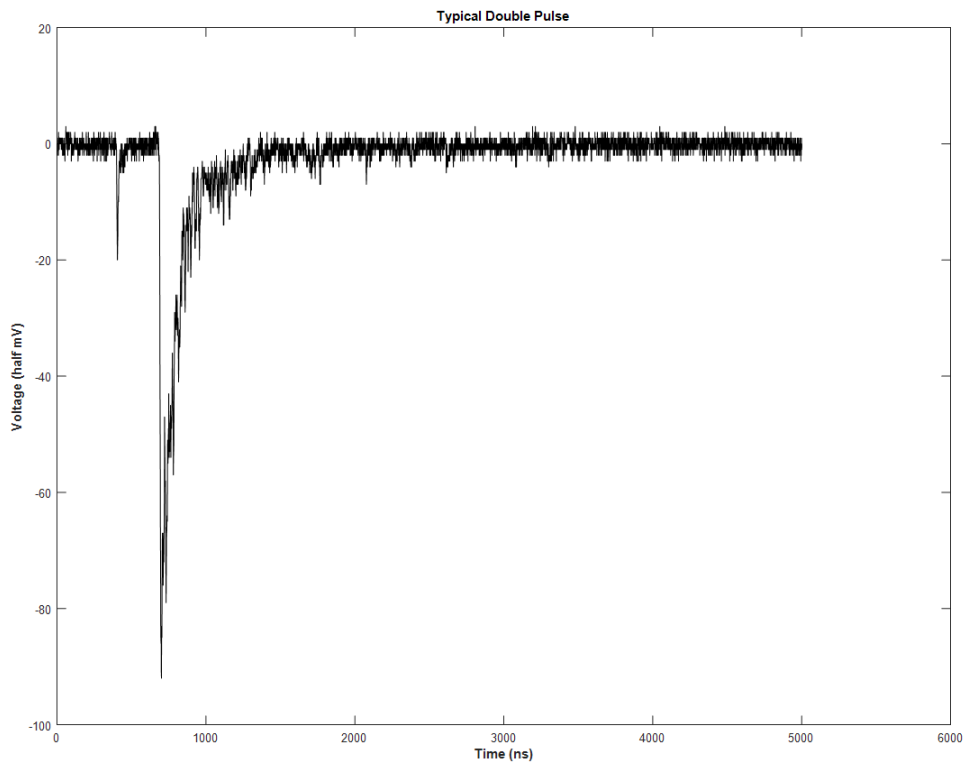
Figure 2.18 Light Pulses detected by the PMT from the two scintillating materials. The narrower pulse on the left is the proton recoil, and the much larger pulse is the neutron capture. Without the neutron capture, the proton recoil can be mistaken for a gamma.

the LGB scintillator. With a reduced speed, the neutron is much more likely to interact with the LGB molecules in the form of a neutron-capture. Upon capturing neutrons, ^{6}Li and ^{10}B release a broad light pulse detected by the PMT. This pulse is much wider than the proton recoil pulse mentioned above; their differences can be seen in Figure 2.18. With both pulses present, one can safely conclude that neutrons are being emitted: a necessity of nuclear reactions.

2.4   Summary

The majority of the work in this project has been to assemble this vacuum system. It was built in such a way as to reduce contaminants as much as possible, by coupling the two chambers together while keeping them isolated with a stopper. Also included in this vacuum system is the equipment needed to detect both charged particles and neutrons, two common fusion products.

Chapter 3

Results and Conclusions

3.1 Results

3.1.1 Charged Particle Detection

Here I explain and compare the data obtained with the charged particle detectors. As mentioned in Chapter 2, I did two runs with the detectors: one at room temperature and the other with them chilled. Recall from Figure 2.14, that alpha particles tend to deposit more of their energy in the first detector, thus on a graph of energies, we would expect to see more activity in the upper left part of the graph. Which is precisely what we see in Figures 3.1 and 3.2. Furthermore, it is evident when comparing them that Figure 3.2 has much less spread; this is precisely the reaction we would expect when reducing noise through cooling of the detectors.

3.1.2 Thermal Deposition results

After the system was completed, I attempted several depositions. The first was unsuccessful: upon venting the film to atmosphere the deposited material peeled itself off the wafer. This was likely due to it's quick exposure to water in the atmosphere. The second attempt however was a success.
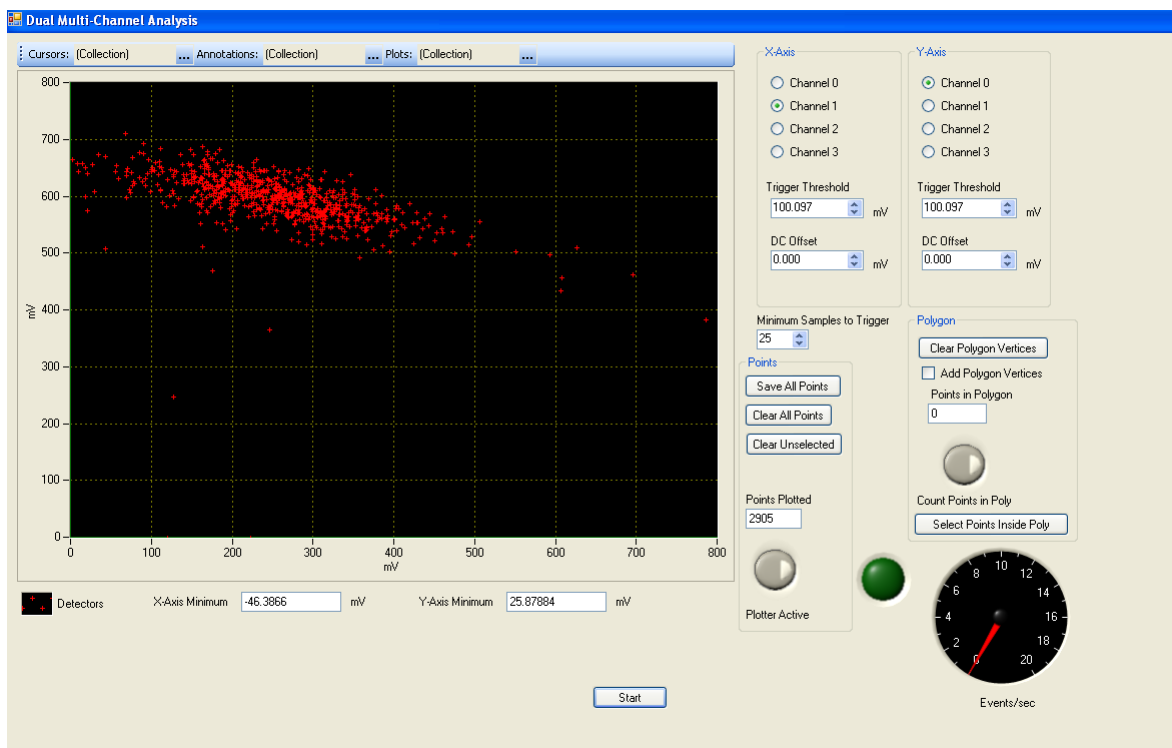
Figure 3.1 Data obtained from the set-up shown in Figure 2.16. The y-axis relates to ΔE and the x-axis to E, just like Figure 2.15. A comparison of the two figures shows a similar curve.
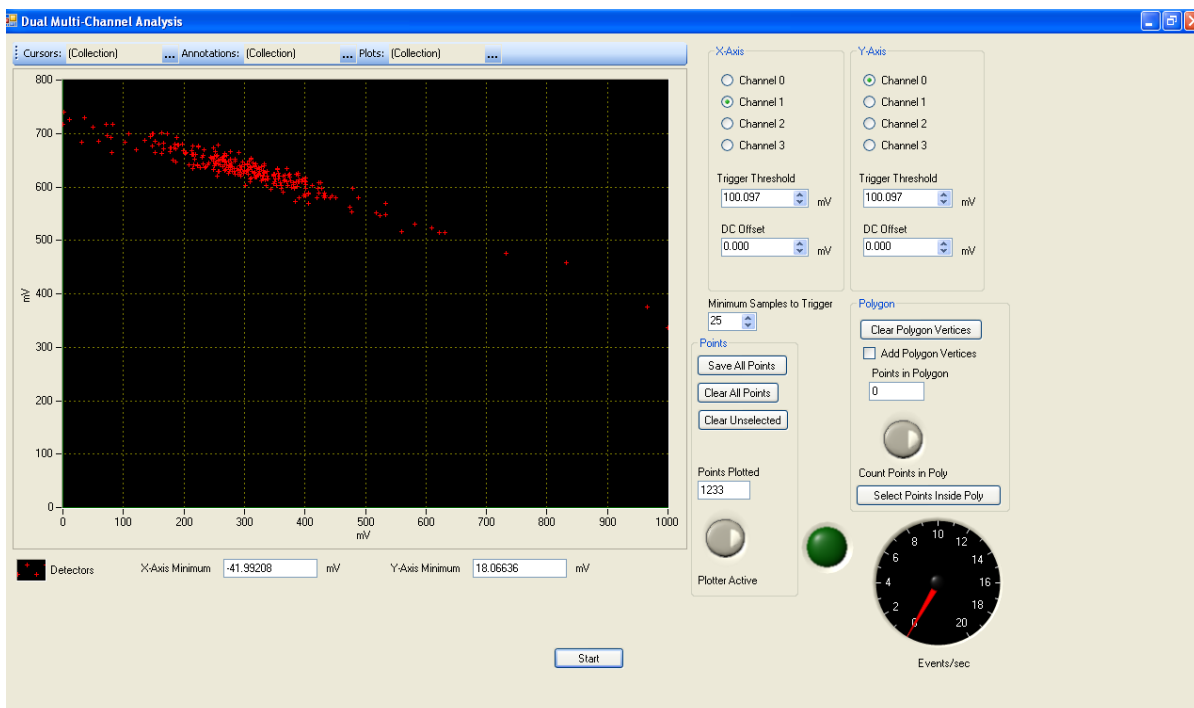
Figure 3.2 After chilling the telescope with liquid nitrogen for a few minutes, this data was taken. Comparison of this graph to Figure 3.1 shows a similar shape, but this graph has much less spread, and thus the detectors are much more accurate when chilled.
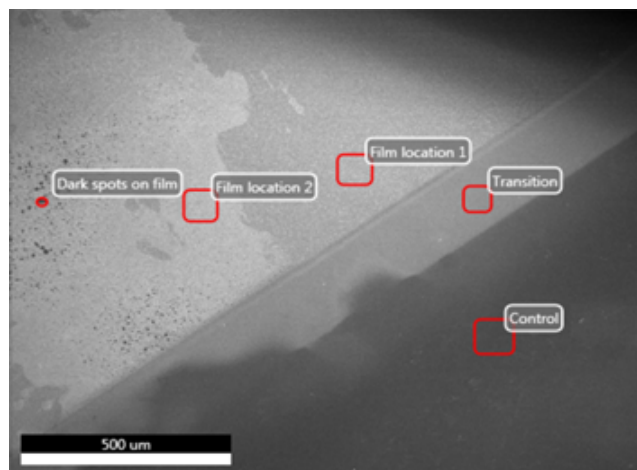
Figure 3.3 A magnified view of the Ca film using an SEM. The following five figures are basic composition analysis of the five red outlined areas.

After which, the sample was taken to be analyzed at the Scanning Electron Microscope (SEM) in U178. Five areas of the sample were analyzed to determine their basic composition. The first analyzed area, Figure 3.4, was free of the Ca deposition because the clip used to attach the film to the handle covered this section of the film, causing the film itself to avoid deposition. As a result, this are was called the control, as it gives the composition of the Si wafer itself. Figures 3.4 through 3.8 show those five analyzed areas. It is important to note, that in those figures, the Kratio, Z, R, A and F are parameters used by the SEM to fit the data. In addition, the Error % isa percentage of the Atomic %. In Figure 3.4 for example, the Error % of Carbon means that 35% of the 2.3% is the error, as opposed to the error being $2.3\% \pm 35\%$.

3.2 Conclusion and future work

Though the ultimate goal of this project has yet to be completed, I am proud of the work I have done in preparing the way for others to complete this project. It is safe to say that both the detection system is fully functional. As far as the deposition system is concerned, my successful deposition showed it is also functional, but certain aspects of the process, such as how long to deposit and at
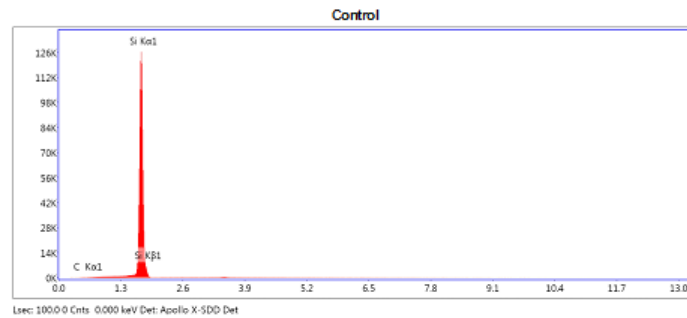
Figure 3.4 Since the clip covered this section of the wafer, the Si content is much higher than in the following areas.

Figure 3.5

Film location 1

Lsec: 100.00 Cnts 0.000 keV Det: Apollo X-SDD Det
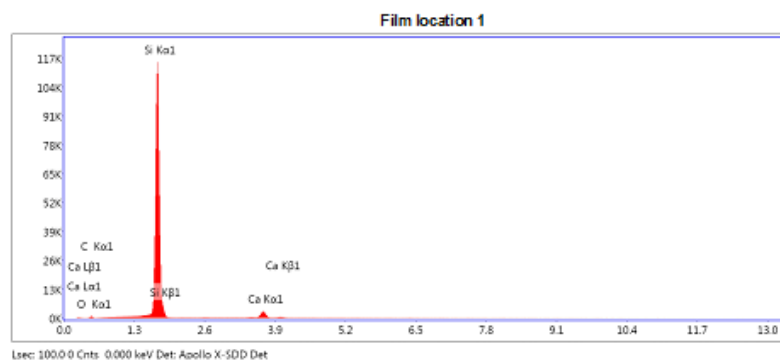
eZAF Smart Quant Results

Element	Weight %	Atomic %	Net Int.	Error %	Kratio	Z	R	A	F
C K	4.93	10.66	8.91	16.50	0.0042	1.1322	0.9292	0.0760	1.0000
O K	4.49	7.28	41.93	11.51	0.0072	1.0860	0.9521	0.1486	1.0000
SIK	84.48	78.11	9534.96	1.63	0.7933	0.9908	1.0027	0.9453	1.0025
CaK	6.10	3.96	303.41	4.39	0.0470	0.9368	1.0386	0.8093	1.0148

Figure 3.6

Film location 2

Lsec: 100.00 Cnts 0.000 keV Det: Apollo X-SDD Det
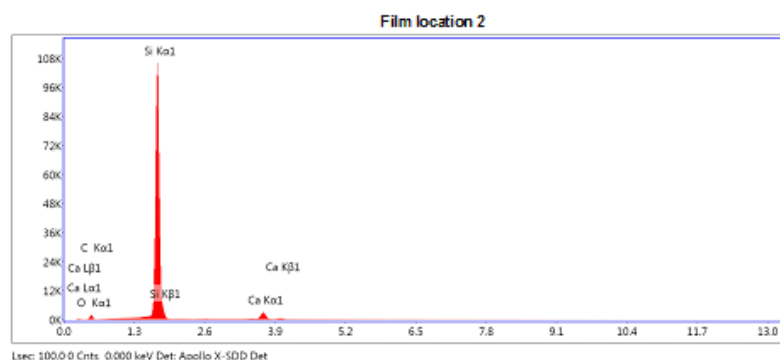
eZAF Smart Quant Results

Element	Weight %	Atomic %	Net Int.	Error %	Kratio	Z	R	A	F
C K	5.00	10.29	9.79	16.48	0.0045	1.1246	0.9333	0.0808	1.0000
O K	11.35	17.54	115.36	10.38	0.0194	1.0785	0.9559	0.1584	1.0000
SIK	77.98	68.67	8717.01	1.90	0.7061	0.9836	1.0060	0.9183	1.0026
CaK	5.67	3.50	292.17	4.23	0.0440	0.9298	1.0414	0.8230	1.0152

Figure 3.7

Dark spots on film

Lsec: 100.0 0 Cnts 0.000 keV Det: Apollo X-SDD Det

eZAF Smart Quant Results

Element	Weight %	Atomic %	Net Int.	Error %	Kratio	Z	R	A	F
C K	4.97	10.05	9.91	16.71	0.0046	1.1217	0.9349	0.0824	1.0000
O K	13.95	21.17	146.13	10.21	0.0245	1.0757	0.9575	0.1636	1.0000
SiK	75.83	65.58	8382.67	1.99	0.6784	0.9808	1.0074	0.9098	1.0026
ClK	0.09	0.06	4.79	46.05	0.0005	0.9144	1.0264	0.5766	1.0096
CaK	5.16	3.13	266.75	4.27	0.0402	0.9271	1.0425	0.8273	1.0155

Figure 3.8

what temperature have yet to be determined.

The large majority of my work has been the assembly and (to some degree) the manufacturing of the vacuum system. Since its assembly, I have leak tested and baked out the system several times and now it can now consistently reach a pressure of $2~\mu$Torr. The reliability of the system indicates there are no significant leaks, even when adjusting the push rods for example. In addition, both the Ion gauge and the magnetron agree with each other very well, so I am confident they are accurate.

Just as my work has been aided by those before me, this project will enable those after me to continue with this research. First and foremost, the next step will be to work on the particle accelerator itself to ensure it is functional. After which, I expect various materials to be prepared and tested, using this vacuum system, to find their screening potentials. By comparing those potentials with others published in literature, one can verify the accuracy of our equipment. It is important to note that evaporating at certain rates can yield a smoother thin film surface. Therefore, by testing

the same material prepared in different ways, if the screening changes significantly based on the preparation method, it may signify that the screening potential does indeed depend on the target's surface; and their may be a correlation between the number of voids and screening potentials.

List of Figures

Appendix A

Appendix

A.1   Screening Potentials

The following is a table of the screening potentials of various materials acquired from numerous sources. All of the values listed are specific to deuterium-deuterium fusion.

Table A.1 Electron Screening Potentials

Target	Ue (eV)	Source	Target
6LiI	235	Fang, J. Phys. Soc. Jpn. 80, 084201	6LiI
7LiI	140	Fang, J. Phys. Soc. Jpn. 80, 084201	7LiI
Ag	330	Raoila, Eur. Phys. J. A 19, 283	Ag
Ag	23	Bonomo, Nucl. Phys. A 719, 37	Ag
Al	520	Bonomo, Nucl. Phys. A 719, 37	Al
Al	520	Raoila, Eur. Phys. J. A 19, 283	Al
Al	190	Huke, Phys. Rev. C 78, 015803	Al
Al2O3	30	Bonomo, Nucl. Phys. A 719, 37	Al2O3
Al2O3	30	Raoila, Eur. Phys. J. A 19, 283	Al2O3
AlD	191	Czerski, Europhys. Lett. 68, 363	AlD
AlD	190	Czerski, Nucl. Instrum. Methods Phys. Res. B 193, 183	AlD
AlD0.8	190	Huke, Phys. Rev. C 78, 015803	AlD0.9
Au	280	Raoila, Eur. Phys. J. A 19, 283	Au
Au	70	Kasagi, J. Phys. Soc. Jpn. 71, 2881	Au
Au	70	Kasagi, Surf. Coat. Tech. 201, 8574	Au
Au	61	Bonomo, Nucl. Phys. A 719, 37	Au
B	30	Bonomo, Nucl. Phys. A 719, 37	B
B	30	Raoila, Eur. Phys. J. A 19, 283	B
Ba	490	Raoila, Eur. Phys. J. A 19, 283	Ba

Target	Ue (eV)	Source	Target
Be	180	Bonomo, Nucl. Phys. A 719, 37	2003
Be	180	Raoila, Eur. Phys. J. A 19, 283	2004
BeO	30	Bonomo, Nucl. Phys. A 719, 37	2003
BeO	30	Raoila, Eur. Phys. J. A 19, 283	2004
Bi	540	Raoila, Eur. Phys. J. A 19, 283	2004
C	60	Raoila, Eur. Phys. J. A 19, 283	2004
C	52	Bonomo, Nucl. Phys. A 719, 37	2003
C	50	Raiola, Eur. Phys. J. A 27, 79	2006
C	0	Huke, Phys. Rev. C 78, 015803	2008
CaO2	50	Raoila, Eur. Phys. J. A 19, 283	2004
Cd	390	Bonomo, Nucl. Phys. A 719, 37	2003
Cd	360	Raoila, Eur. Phys. J. A 19, 283	2004
CD	-20	Czerski, Nucl. Instrum. Methods Phys. Res. B 193, 183	2002
CD2	40	Bystritsky Phys. Atomic Nuclei Vol. 75 No.1	2012
Ce	200	Raiola, Eur. Phys. J. A 27, 79	2006
Ce	30	Raiola, Eur. Phys. J. A 19, 283	2004
Co	640	Bonomo, Nucl. Phys. A 719, 37	2003
Co	640	Raoila, Eur. Phys. J. A 19, 283	2004
Co	640	Raiola, Eur. Phys. J. A 27, 79	2006
Co	480	Raiola, Eur. Phys. J. A 27, 79	2006

Target	Ue (eV)	Source	Target
Cr	320	Raoila, Eur. Phys. J. A 19, 283	2004
Cr	220	Bonomo, Nucl. Phys. A 719, 37	2003
Cu	470	Raoila, Eur. Phys. J. A 19, 283	2004
Cu	120	Kasagi, Surf. Coat. Tech. 201, 8574	2007
Cu	43	Bonomo, Nucl. Phys. A 719, 37	2003
D2O	25	Bystritsky Phys. Atomic Nuclei Vol. 75 No.1	2012
Dy	340	Raiola, Eur. Phys. J. A 27, 79	2006
Dy	30	Raoila, Eur. Phys. J. A 19, 283	2004
DyDx	50	Bonomo, Nucl. Phys. A 719, 37	2003
Er	360	Raiola, Eur. Phys. J. A 27, 79	2006
Er	50	Raoila, Eur. Phys. J. A 19, 283	2004
ErDx	50	Bonomo, Nucl. Phys. A 719, 37	2003
Eu	120	Raiola, Eur. Phys. J. A 27, 79	2006
Eu	50	Raoila, Eur. Phys. J. A 19, 283	2004
Fe	460	Raoila, Eur. Phys. J. A 19, 283	2004
Fe	450	Bonomo, Nucl. Phys. A 719, 37	2003
Fe	200	Kasagi, J. Phys. Soc. Jpn. 71, 2881	2002
Fe	200	Kasagi, Surf. Coat. Tech. 201, 8574	2007
Gd	340	Raiola, Eur. Phys. J. A 27, 79	2006
Gd	50	Raoila, Eur. Phys. J. A 19, 283	2004

Target	Ue (eV)	Source	Target
Ge	80	Raoila, Eur. Phys. J. A 19, 283	2004
Ge	60	Bonomo, Nucl. Phys. A 719, 37	2003
H2/D2g	440	Engstler, Z. Phys. A 342, 471	1992
H2/D2g	330	Engstler, Z. Phys. A 342, 471	1992
H2/D2g	300	Engstler, Z. Phys. A 342, 471	1992
H2/D2g	218	Wang, J. Phys. G: Nucl. Part. Phys. 39, 015201	2012
Hf	370	Raiola, Eur. Phys. J. A 27, 79	2006
Hf	30	Raoila, Eur. Phys. J. A 19, 283	2004
HfDx	87	Bonomo, Nucl. Phys. A 719, 37	2003
Ho	165	Raiola, Eur. Phys. J. A 27, 79	2006
Ho	70	Raoila, Eur. Phys. J. A 19, 283	2004
In	520	Raoila, Eur. Phys. J. A 19, 283	2004
Ir	200	Bonomo, Nucl. Phys. A 719, 37	2003
Ir	200	Raoila, Eur. Phys. J. A 19, 283	2004
La	245	Raiola, Eur. Phys. J. A 27, 79	2006
La	60	Raoila, Eur. Phys. J. A 19, 283	2004
Li	150	Huke, Phys. Rev. C 78, 015803	2008
Li	150	Huke, Phys. Rev. C 78, 015803	2008
LiF	470	Engstler, Z. Phys. A 342, 471	1992
LiF	380	Engstler, Z. Phys. A 342, 471	1992

Target	Ue (eV)	Source	Target
LiF	310	Wang, J. Phys. G: Nucl. Part. Phys. 39, 015201	2012
LiF	300	Engstler, Z. Phys. A 342, 471	1992
Lil	543	Toriyabe, Phys. Rev. C 85, 054620	2012
Lu	265	Raiola, Eur. Phys. J. A 27, 79	2006
Lu	40	Raoila, Eur. Phys. J. A 19, 283	2004
Mg	440	Bonomo, Nucl. Phys. A 719, 37	2003
Mg	440	Raoila, Eur. Phys. J. A 19, 283	2004
Mn	390	Raoila, Eur. Phys. J. A 19, 283	2004
Mn	350	Bonomo, Nucl. Phys. A 719, 37	2003
Mo	420	Raoila, Eur. Phys. J. A 19, 283	2004
Mo	220	Bonomo, Nucl. Phys. A 719, 37	2003
Nb	470	Raoila, Eur. Phys. J. A 19, 283	2004
Nb	400	Bonomo, Nucl. Phys. A 719, 37	2003
Nd	190	Raiola, Eur. Phys. J. A 27, 79	2006
Nd	30	Raoila, Eur. Phys. J. A 19, 283	2004
Ni	450	Bonomo, Nucl. Phys. A 719, 37	2003
Ni	380	Raoila, Eur. Phys. J. A 19, 283	2004
Ni	80	Kasagi, Surf. Coat. Tech. 201, 8574	2007
Pb	480	Raoila, Eur. Phys. J. A 19, 283	2004
Pb	440	Bonomo, Nucl. Phys. A 719, 37	2003

Target	Ue (eV)	Source	Target
Pd	800	Bonomo, Nucl. Phys. A 719, 37	2003
Pd	800	Raoila, Eur. Phys. J. A 19, 283	2004
Pd	310	Kasagi, J. Phys. Soc. Jpn. 71, 2881	2002
Pd	310	Kasagi, Surf. Coat. Tech. 201, 8574	2007
Pd0.3	313	Huke, Phys. Rev. C 78, 015803	2008
PdD0.2	296	Czerski, Europhys. Lett. 68, 363	2004
PdO	600	Kasagi, J. Phys. Soc. Jpn. 71, 2881	2002
PdO	600	Kasagi, Surf. Coat. Tech. 201, 8574	2007
Pr	70	Raoila, Eur. Phys. J. A 19, 283	2004
PrDx	78	Bonomo, Nucl. Phys. A 719, 37	2003
Pt	680	Rolfs, Prog. Theor. Phys. Supplement 154, 373	2004
Pt	675	Raiola, Eur. Phys. J. A 27, 79	2006
Pt	670	Raoila, Eur. Phys. J. A 19, 283	2004
Pt	530	Raiola, Eur. Phys. J. A 27, 79	2006
Pt	530	Raiola, Eur. Phys. J. A 27, 79	2006
Pt	480	Raiola, Eur. Phys. J. A 27, 79	2006
Pt	465	Raiola, Eur. Phys. J. A 27, 79	2006
Pt	440	Bonomo, Nucl. Phys. A 719, 37	2003
PtDx	730	Bonomo, Nucl. Phys. A 719, 37	2003
Re	420	Bonomo, Nucl. Phys. A 719, 37	2003

Target	Ue (eV)	Source	Target
Re	230	Raoila, Eur. Phys. J. A 19, 283	2004
Re	200	Kasagi, Surf. Coat. Tech. 201, 8574	2007
Rh	230	Bonomo, Nucl. Phys. A 719, 37	2003
Rh	230	Raoila, Eur. Phys. J. A 19, 283	2004
Ru	220	Bonomo, Nucl. Phys. A 719, 37	2003
Ru	215	Raoila, Eur. Phys. J. A 19, 283	2004
Sb	720	Raoila, Eur. Phys. J. A 19, 283	2004
Sc	320	Raiola, Eur. Phys. J. A 27, 79	2006
Sc	30	Raoila, Eur. Phys. J. A 19, 283	2004
ScDx	30	Bonomo, Nucl. Phys. A 719, 37	2003
Si	60	Raoila, Eur. Phys. J. A 19, 283	2004
Si	45	Bonomo, Nucl. Phys. A 719, 37	2003
Sm	520	TS Wang, J. Phys. G: Nucl. Part. Phys. 34 2255	2007
Sm	314	Raiola, Eur. Phys. J. A 27, 79	2006
Sm	30	Raoila, Eur. Phys. J. A 19, 283	2004
SmDx	30	Bonomo, Nucl. Phys. A 719, 37	2003
Sn	200	Bonomo, Nucl. Phys. A 719, 37	2003
Sn	130	Raoila, Eur. Phys. J. A 19, 283	2004
Sr	350-800	Huke, Phys. Rev. C 78, 015803	2008
Sr	210	Raoila, Eur. Phys. J. A 19, 283	2004

Target	Ue (eV)	Source	Target
SrD1.0	350-800	Huke, Phys. Rev. C 78, 015803	2008
Ta	340	Bonomo, Nucl. Phys. A 719, 37	2003
Ta	322	Huke, Phys. Rev. C 78, 015803	2008
Ta	270	Raoila, Eur. Phys. J. A 19, 283	2004
TaD	322	Czerski, Nucl. Instrum. Methods Phys. Res. B 193, 183	2002
TaD	302	Czerski, Europhys. Lett. 68, 363	2004
TaD	136	Czerski, Eur. Phys. J. A 27, 83	2006
TaD0.13	340	Bonomo, Nucl. Phys. A 719, 37	2003
TaD0.13	309	Raiola, Eur. Phys. J. A 13, 377	2002
TaD0.13	270	Raiola, Eur. Phys. J. A 19, 283	2004
TaD0.5	313	Bystritsky, Nuc. Phys. A 889, 93-104	2012
TaD0.9	322	Huke, Phys. Rev. C 78, 015803	2008
Tb	340	Raiola, Eur. Phys. J. A 27, 79	2006
Tb	30	Raoila, Eur. Phys. J. A 19, 283	2004
Ti	295	Raiola, Eur. Phys. J. A 27, 79	2006
Ti	290	Raiola, Eur. Phys. J. A 27, 79	2006
Ti	250	Raiola, Eur. Phys. J. A 27, 79	2006
Ti	65	Kasagi, J. Phys. Soc. Jpn. 71, 2881	2002
Ti	65	Kasagi, Surf. Coat. Tech. 201, 8574	2007
Ti	50	Raiola, Eur. Phys. J. A 27, 79	2006

Target	Ue (eV)	Source	Target
Ti	30	Raoila, Eur. Phys. J. A 19, 283	2004
Ti	30	Raiola, Eur. Phys. J. A 27, 79	2006
Ti	19	Yuki, J. Phys. G: Nucl. Part. Phys. 23, 1459	1997
TiD0.23	295	Raiola, Eur. Phys. J. A 27, 79 (and references therein)	2006
TiD0.26	250	Raiola, Eur. Phys. J. A 27, 79 (and references therein)	2006
TiD1.1	50	Raiola, Eur. Phys. J. A 27, 79 (and references therein)	2006
TiD1.3	100	Czerski, Eur. Phys. J. A 27, 83	2006
TiD1.3	30	Raiola, Eur. Phys. J. A 19, 283	2004
TiD1.73	131	Bystritsky, Pis'ma v Zhurnal Vol. 99 No. 9	2014
TiD2	125	Bystritsky, Nuc. Phys. A 889, 93-104	2012
TiD2	125	Bystritsky Phys. Atomic Nuclei Vol. 75 No.1	2012
TiD3.76	66	Kasagi, J. Phys. Soc. Jpn. 71, 2881	2002
TiDx	30	Bonomo, Nucl. Phys. A 719, 37	2003
TiO2	160-750	Bagulya, Phys. Scr. 90 074051	2015
Tl	550	Bonomo, Nucl. Phys. A 719, 37	2003
Tl	550	Raoila, Eur. Phys. J. A 19, 283	2004
Tm	260	Raiola, Eur. Phys. J. A 27, 79	2006
Tm	70	Raoila, Eur. Phys. J. A 19, 283	2004
V	480	Raoila, Eur. Phys. J. A 19, 283	2004
V	350	Bonomo, Nucl. Phys. A 719, 37	2003

Target	Ue (eV)	Source	Target
W	250	Raoila, Eur. Phys. J. A 19, 283	2004
W	220	Bonomo, Nucl. Phys. A 719, 37	2003
Y	320	Bonomo, Nucl. Phys. A 719, 37	2003
Y	270	Raiola, Eur. Phys. J. A 27, 79	2006
Y	70	Raoila, Eur. Phys. J. A 19, 283	2004
Yb	110	Raiola, Eur. Phys. J. A 27, 79	2006
Yb	81	Yuki, J. Phys. G: Nucl. Part. Phys. 23, 1459	1997
Yb	80	Kasagi, Surf. Coat. Tech. 201, 8574	2007
Yb	40	Raoila, Eur. Phys. J. A 19, 283	2004
YbDx	40	Bonomo, Nucl. Phys. A 719, 37	2003
Zn	480	Bonomo, Nucl. Phys. A 719, 37	2003
Zn	480	Raoila, Eur. Phys. J. A 19, 283	2004
Zr	319	K Czerski, J. Phys. G: Nucl. Part. Phys. 35 014012	2007
Zr	297	Huke, Phys. Rev. C 78, 015803	2008
Zr	205	Raiola, Eur. Phys. J. A 27, 79	2006
Zr	40	Raoila, Eur. Phys. J. A 19, 283	2004
ZrD0.13	205	Raiola, Eur. Phys. J. A 27, 79 (and references therein)	2006
ZrD1.1	40	Raiola, Eur. Phys. J. A 19, 283	2004
ZrD2	319	Czerski, J. Phys. G: Nucl. Part. Phys. 35 014012	2008
ZrD2	297	Czerski, Nucl. Instrum. Methods Phys. Res. B 193, 183	2002

Target	Ue (eV)	Source	Target
ZrD2	297	Czerski, Eur. Phys. J. A 27, 83	2006
ZrD2	295	Czerski, Europhys. Lett. 68, 363	2004
ZrD2	205	Bystritsky, Nucl. Phys. A 889 93-104	2012
ZrD2	112	Czerski, Eur. Phys. J. A 27, 83	2006
ZrD2.1	297	Huke, Phys. Rev. C 78, 015803	2008
ZrDx	83	Bonomo, Nucl. Phys. A 719, 37	2003

A.2 3d Design

The following are the 3D designs of the vacuum system creating using the student edition of Design

Spark. Refer to Chapter 2 to see pictures of the completed system.
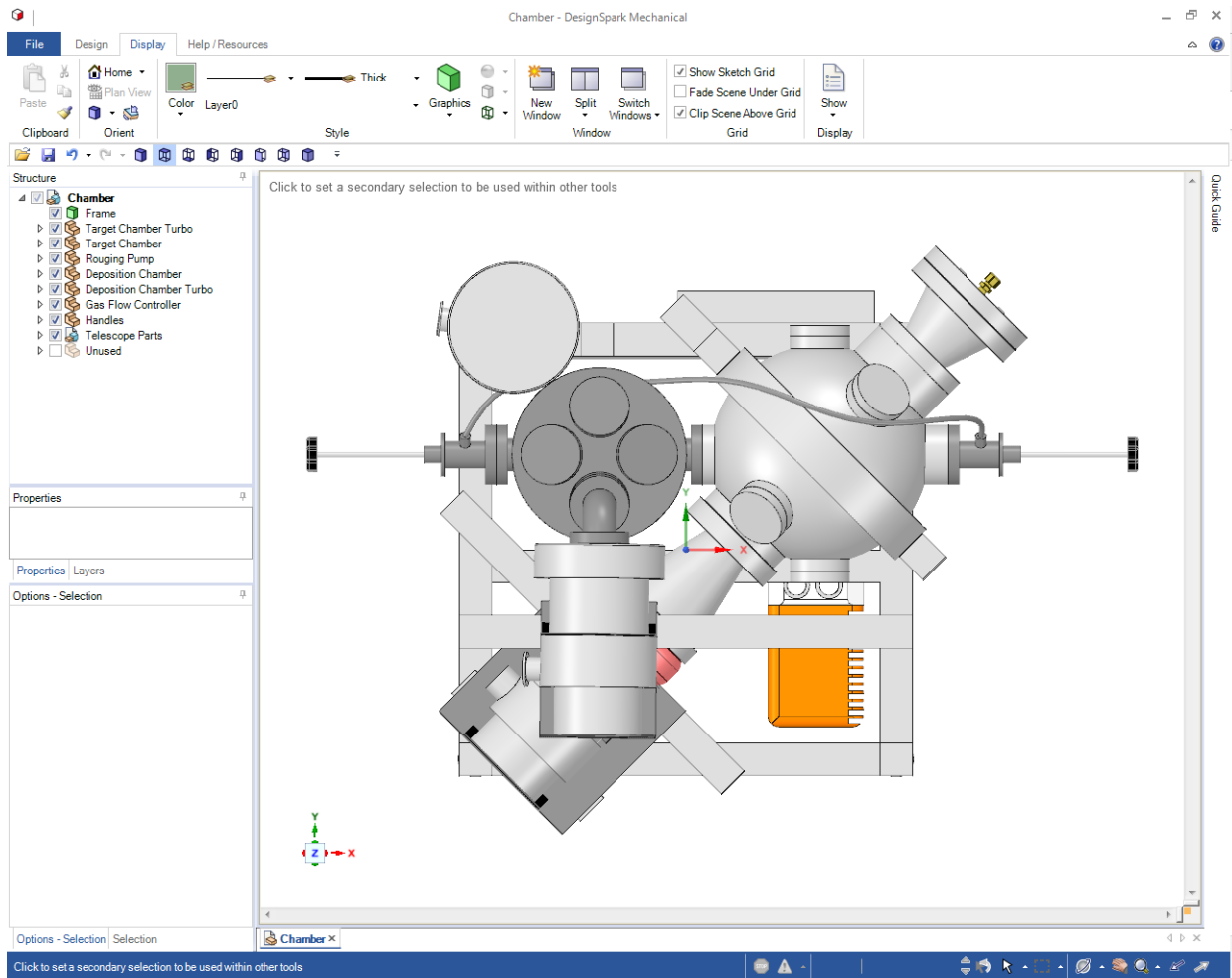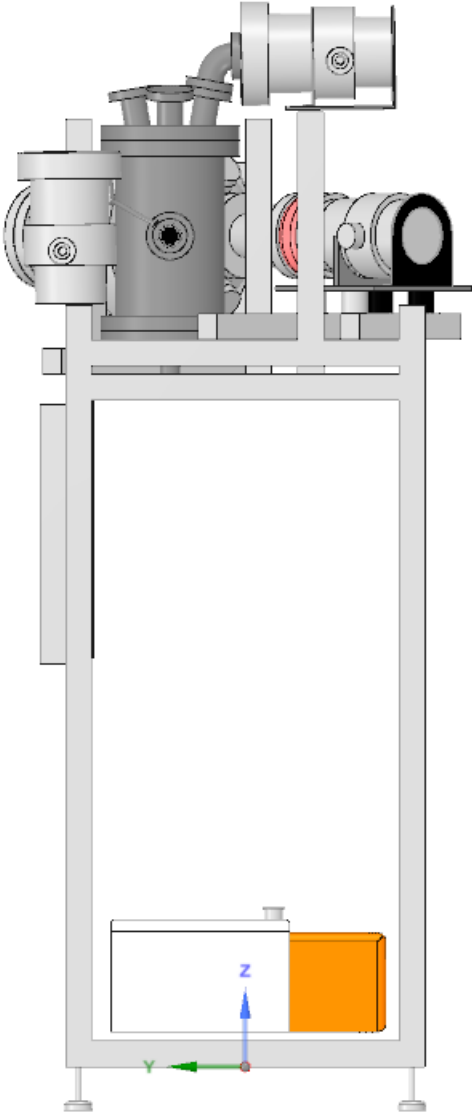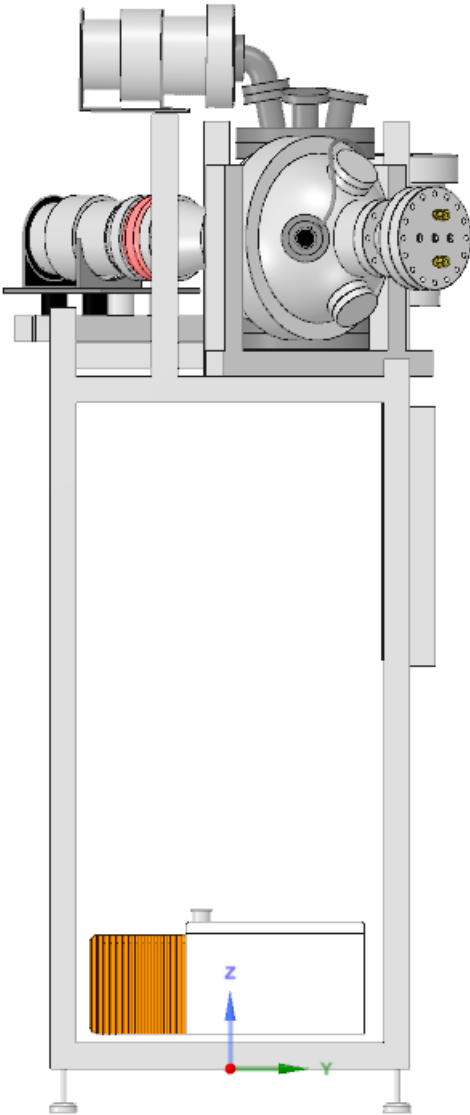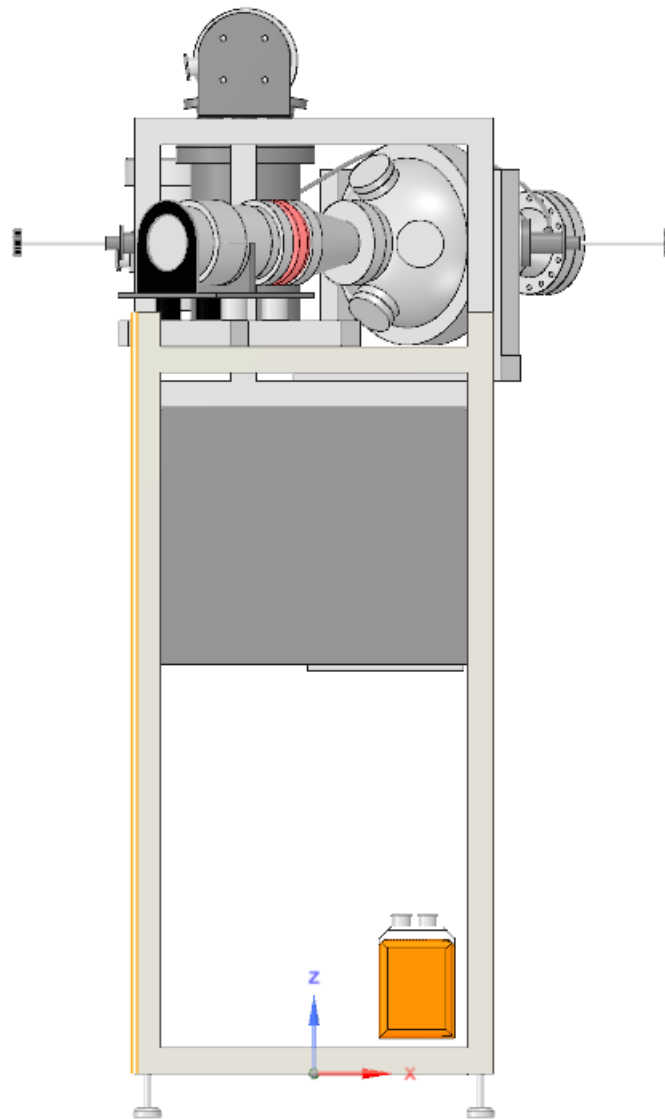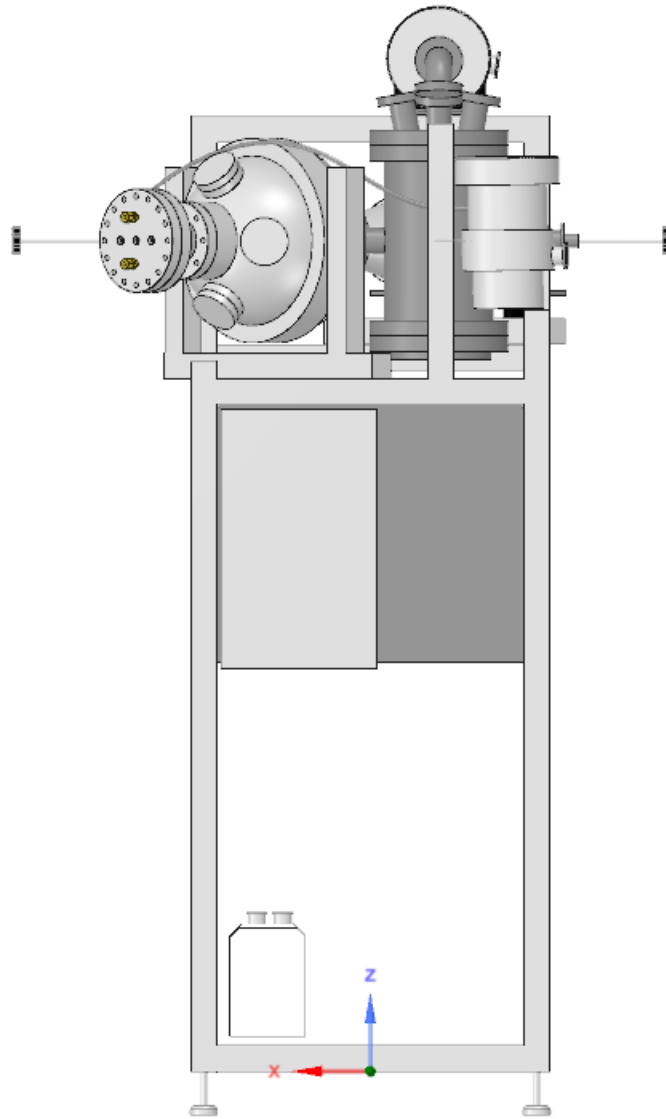
A.3   Frame Construction

This section explains the methods used to construct the frame to hold the chamber. I used 1.5"

Aluminum T-Slot from Global Industrial and 80-20 Inc. Originally they were connected at right

angles using an elbow, but that was not sturdy enough. The method tf using the replacement pieces

is as follow In place of the elbow, I drilled with a $\frac{13}{16}$" endmill approximately .625 inches deep and

.75 inches above the edge of the T-slot on both sides of the bar. The circular piece that holds the bolt can then be inserted into either hole. The long, straight nut can then be connected to the bolts, and that slides directly into the slot of another beam. After both bolts are securely tightened, it is a very steady connection.

A.4   Magnetron Schematic

The schematic I used when wiring the magnetron to give it power and obtain its output voltage.

Figure 1 - General view of the AIM Gauge (showing the NW25 flange)

Introduction

AIW1571/B

1. End-cap
2. Vacuum flange
3. Body tube
4. Magnet housing
5. Cable connector plug
6. Set-point potentiometer (on end of item 1)
7. AIM Gauge connector socket

A.5   Magnetron Pressure Output vs. Voltage
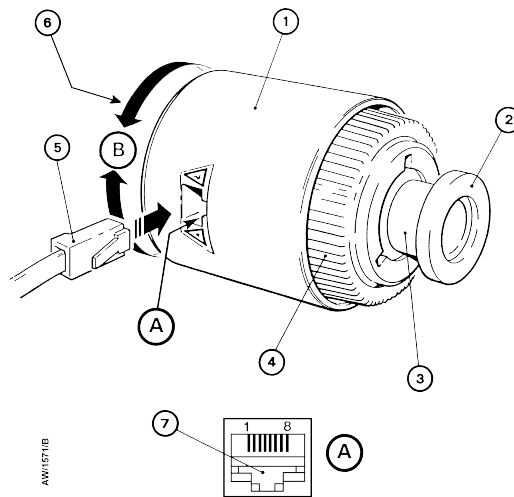
The magnetron's output voltage can be converted to pressure using this table.

D146-41-880 Issue J

EDWARDS

Operation

Table 2 - Pressure and voltage characteristics for nitrogen and dry air: AIM-S and AIM-SL Gauges

Pressure (mbar)	Output voltage (V)	Pressure (torr)	Pressure (mbar)	Output voltage (V)	Pressure (torr)
1.0×10^{-8}	2.00	7.5×10^{-9}	6.9×10^{-6}	6.40	5.2×10^{-6}
2.4×10^{-8}	2.50	1.8×10^{-8}	8.4×10^{-6}	6.60	6.3×10^{-6}
5.8×10^{-8}	3.00	4.4×10^{-8}	1.0×10^{-5}	6.80	7.5×10^{-6}
8.1×10^{-8}	3.20	6.1×10^{-8}	1.2×10^{-5}	7.00	9.0×10^{-6}
1.1×10^{-7}	3.40	8.3×10^{-8}	1.4×10^{-5}	7.20	1.1×10^{-5}
1.5×10^{-7}	3.60	1.1×10^{-7}	1.7×10^{-5}	7.40	1.3×10^{-5}
2.1×10^{-7}	3.80	1.6×10^{-7}	2.0×10^{-5}	7.60	1.5×10^{-5}
2.9×10^{-7}	4.00	2.2×10^{-7}	2.4×10^{-5}	7.80	1.8×10^{-5}
4.0×10^{-7}	4.20	3.0×10^{-7}	2.9×10^{-5}	8.00	2.2×10^{-5}
5.4×10^{-7}	4.40	4.1×10^{-7}	3.5×10^{-5}	8.20	2.6×10^{-5}
7.3×10^{-7}	4.60	5.5×10^{-7}	4.3×10^{-5}	8.40	3.2×10^{-5}
9.8×10^{-7}	4.80	7.4×10^{-7}	5.7×10^{-5}	8.60	4.3×10^{-5}
1.3×10^{-6}	5.00	9.8×10^{-7}	7.9×10^{-5}	8.80	5.9×10^{-5}
1.7×10^{-6}	5.20	1.3×10^{-6}	1.2×10^{-4}	9.00	9.0×10^{-5}
2.2×10^{-6}	5.40	1.7×10^{-6}	1.9×10^{-4}	9.20	1.4×10^{-4}
2.8×10^{-6}	5.60	2.1×10^{-6}	3.3×10^{-4}	9.40	2.5×10^{-4}
3.6×10^{-6}	5.80	2.7×10^{-6}	6.7×10^{-4}	9.60	5.0×10^{-4}
4.5×10^{-6}	6.00	3.4×10^{-6}	1.7×10^{-3}	9.80	1.3×10^{-3}
5.6×10^{-6}	6.20	4.2×10^{-6}	3.6×10^{-3}	9.90	2.7×10^{-3}
			1.0×10^{-2}	10.00	7.5×10^{-3}

4.4   Set-point

Note: The set-point is not used if you connect the AIM Gauge to a Edwards AGC Controller or AGD Display.

To adjust the voltage at which the set-point output signal goes on, turn the set-point potentiometer, which is accessible through an access hole in the end-cap of the gauge: see Figure 1. Turn the potentiometer clockwise to increase the voltage and turn it anticlockwise to decrease the voltage. Refer to Section 4.3 to determine the operating voltage which corresponds to a given pressure.

The AIM Gauge has an error monitoring facility, which ensures that the set-point output signal is off:

- When the Gauge is switched off (that is, not enabled).

- For 0.5 seconds immediately after the AIM Gauge is switched on.

- When the pressure output signal is out of range, perhaps because the gauge has failed to strike (ignite).

If required, you can adjust the potentiometer so that the set-point operating voltage is < 1.8 V (that is, turn the potentiometer fully anticlockwise). This ensures that the set-point output signal is permanently off.

If required, you can use the set-point output signal to indicate when the Gauge is operating correctly: adjust the potentiometer so that the set-point operating voltage is $\geq$ 10 V (that is, turn the potentiometer fully clockwise). If the Gauge is operating normally, the set-point output signal will then be switched on.

Note: If you adjust the set-point operating voltage to > 9.5 V, the hysteresis voltage will be > 10 V and the set-point output signal may not switch off when the pressure rises; if so, the set-point output signal will only go off when the gauge is switched off (that is, disabled).

A.6   Americium 2 41: Alpha Energies and Calibration

Information from our Americium 241 source used to calibrate the detectors. The energies of the alphas are of particular importance.

AMERICIUM-241
[^{241}Am]

PHYSICAL DATA

- Gamma Energy: 60 keV (36%)
  (x-rays from Ba-137m)   18 keV (18%)
                                    14 keV (13%)
- Beta Energy: no beta
- Alpha Energy: 5486 keV (85%)
                                    5443 keV (13%)
                                    5388 keV (1%)

- Physical Half-Life: 432.7 years
- Biological Half-Life: 50 years (bone)
- Effective Half-Life: 45 years (bone)

- Specific Activity: 3.43 Ci/gram 1.27×10^{11} Bq/g
- Specific Gamma Constant: 3.14×10^{-1} mR/hr/mCi 8.48×10^{-5} mSv/hr/MBq
  (@ 1 meter)

RADIOLOGICAL DATA

- Radiological Toxicity Rating: Group 1 (very high)
- Critical Organ: Bone
- Routes of Intake: Ingestion, Inhalation, Puncture, Wound, Skin Absorption

- Committed Effective Dose 3.64×10^{3} mrem/uCi 9.84×10^{2} mSv/MBq
  Equivalent (CEDE):   (ingestion)   (ingestion)
                                   4.4×10^{5} mrem/uCi 1.2×10^{5} mSv/MBq
                                   (inhalation)   (inhalation)
- Skin Contamination 1.95×10^{-2}
  (7 mg/cm^2): 7.4×10^{-2} rem/hr/uCi/cm^2 mSv/h/kBq/cm^2
  (Kocher et al)

SHIELDING

- Half-Value Layer (HVL) for lead   <0.04 inches   <0.1 cm
                       HVL for steel   0.04 inches   0.1 cm
- Tenth-Value Layer (TVL) for lead   <0.04 inches   <0.1 cm
                       TVL for steel   0.12 inches   0.3 cm

A.7   Wien Filter Calculations

The following is a Mathematica notebook I used to find the required voltage given a specific B-field.

Wein Filter Calculator

```
In[31]:= (* This program is designed to calculate the
    necesary Voltage to filter specific energies *)
   (* Masses of several isotopes in eV/c^2 *)
   c = 3 * 10 ^ 8;
   Deuterium = 1875.6 * 10^6 / c^2 ;
   Alpha = 3.7273 * 10^9 / c^2 ;
   Hydrogen = 938.79 * 10^6 / c^2 ;
   (* Alter the next two
    parameters based on the experiment *)
   Mass = Deuterium; (* Input the name of the particle *)
   En = 100 * 10 ^ 3;
   (* The Energy of the incoming particle in eV *)

   (* The following are measured values, dont change them *)
   Bf = .132;
   (* The average measured B-field in the filter *)
   R = .0254; (* The measured serpartion
    distance between the conducting plates *)
   V = Bf Sqrt[2 En / Mass] R / 2 ;
   Print["The required voltage is "]
   V
```

The required voltage is

Out[38]= 5193.3

A.8   SRIM Analyzer

The Mathematica file used to analyze the Srim data resulting in Figure 2.15.

```
In[45]:= SetDirectory["D:\\Joe Hall\\Telescope\\Srim Analyzer"];

In[46]:= (* All the files you want to be joined together into one list *)

In[47]:= data5486 = Import["5486 Alph En.dat"];

      data5338 = Import["5338 Alph En.dat"];

      data5443 = Import["5443 Alph En.dat"];

      data5400 = Import["5400 Alph En.dat"];

In[51]:= (* This function eliminates the header from each file,
      eliminates any incomplete lines,
      and extracts the energy value from the dat file *)

In[52]:= datConvert[inData_, totalEnergy_] := Module[{output},
        output = {Transpose[Drop[Drop[inData, 12], -1]][[4]],
          ConstantArray[totalEnergy,
            Length[Transpose[Drop[Drop[inData, 12], -1]][[4]]]]}
       ]

In[53]:= res5486 = datConvert[data5486, 5.486*10^6];

In[54]:= res5338 = datConvert[data5338, 5.338*10^6];

In[55]:= res5443 = datConvert[data5443, 5.443*10^6];

In[56]:= res5400 = datConvert[data5400, 5.400*10^6];

In[57]:= (* Combines all the lists into a new list with two columns *)

      TotalEs =
        Join[res5486[[2]], res5338[[2]], res5443[[2]], res5400[[2]]];
      TotalDelEs = Join[res5486[[1]], res5338[[1]],
          res5443[[1]], res5400[[1]]];

      TotalSet = {TotalEs - TotalDelEs, TotalDelEs};

In[100]:= Labeled[ListPlot[Transpose[TotalSet], PlotRange →
            {{3.9*10^6, 5*10^6}, {0, 1.8*10^6}}, AxesLabel → {"x", "y"}],
          {"E(eV)", "ΔE(eV)"}, {Bottom, Left}, RotateLabel → True];
```

Bibliography

[1] F. Raiola, P. Migliardi, and et al., "Enhanced Electron Screening in d(d,p)t for deuterated Ta," Eur. Phys. J.A **13,** 337–382 (2002).

[2] E. Tsyganov, "Cold nuclear fusion," Physics of Atomic Nuclei **75,** 153–159 (2012).

[3] U. Greife, F. Gorris, M. Junker, C. Rolfs, and D. Zahnow, "Oppenheimer-Phillips effect and electron screening in d+d fusion reactions," Zeitschrift fur Physik A Hadrons and Nuclei **351,** 107–112 (1995).

[4] C. Rolfs and W. Rodney, *Cauldrons in the cosmos* (University of Chicago Press, Chicago, 1998), p. 34124412341235.

[5] K. N. et al., "RPP2011 Muon List," pdg.lbl.gov/2011/listings/rpp2011-list-muon.pdf (Accessed January 25, 2017).

[6] F. Frank, "Hypothetical Alternative Energy Sources for the 'Second Meson' Events," Nature **160,** 525–527 (1947).

[7] L. Alvarez and H. Bradner, "Catalysis of Nuclear Reactions by Mesons," Radition Laboratory, University of California, Berkely, (1956).

[8] J. D. Jackson, "Catalysis of Nuclear Reactions between Hydrogen Isotopes by μ^- Mesons," Phys. Rev. **106,** 330–339 (1957).

[9] S. Jones, K. Watts, A. Caffrey, and J. Walter, "Muon-Catalyzed Fusion Experiment Target And Detector Systems Preliminary Design Report," US Deptartment of Energy EGG-IS-5806 (1982).

[10] L. Kowalski, "Jones' manuscript on history of Cold Fusion at BYU," http://pages.csam.montclair.edu/ kowalski/cf/131history.htm (2004).

[11] C. D. V. Siclen and S. E. Jones, "Piezonuclear fusion in isotopic hydrogen molecules," Journal of Physics G: Nuclear Physics **12,** 213 (1986).

[12] S. Jones and J. Ellsworth, *Geo-Fusion and cold Nucleosynthesis*, 514 ed.

[13] F. Goff and G. M. McMurtry, "Tritium and stable isotopes of magmatic waters," Journal of Volcanology and Geothermal Research **97,** 347–396 (2000).

[14] S. Jones and F. K. et al., *Charged-particle Emissions from Metal Deuterides* (This volume is a collection of papers from the Tenth International Conference on Cold Fusion, 2003).

[15] H. Assenbaum, K. Langanke, and C. Rolfs, "Effects of Electron Screening on Low-Energy Fusion Cross Sections," Z. Phys. A **327,** 461–468 (1987).

[16] V. Lyuboshitz, "Lifetime and path length of the virtual particle," Physics of Atomic Nuclei **68,** 524–527 (2005).

[17] K. Andre and P. Kim, "Carbon Wonderland," http://www.nature.com/scientificamerican/journal/v298/n4/full/ 90.html (Accessed February 1, 2017).

[18] S. Reynaud, A. Lambrecht, C. Genet, and M. Jaekel, "Quantum vacuum fluctuations and dark energy," Astrophysics and Space Science **326,** 7–10 (2001).

[19] P. Davies, *Super Force: The search for a grand unified theory of nature* (Touchstone Press, London, 1984).

[20] H. E. Puthoff, "Ground state of hydrogen as a zero-point-fluctuation-determined state," Physical Review D 35 (1987).

[21] C. Institute, "Quantum Vacuum Energy Extraction," http://www.calphysics.org/zpe.html (Accessed February 1, 2017).

[22] A. R. Kitson, "On the zero-point energy of elliptic-cylindrical and spheroidal boundaries," Ph.D. dissertation (Massey University, New Zealand, 2009).

[23] D. C. Cole and Y. Zou, "Quantum mechanical ground state of hydrogen obtained from classical electrodynamics," Physics Letters A **317,** 14–20 (2003).

[24] J. A. Hutchison, T. Schwartz, C. Genet, E. Devaux, and T. W. Ebbesen, "Modifying chemical landscapes by coupling to vacuum fields," Angewandte Chemie (International ed. in English) **51,** 1592–1628 (2012).

Index